

Uncertainty Quantification for Molecular Property Predictions with Graph Neural Architecture Search

Shengli Jiang^{1*}, Shiyi Qin¹, Reid C. Van Lehn¹, Prasanna Balaprakash² and Victor M. Zavala^{1,3}

¹Department of Chemical and Biological Engineering

University of Wisconsin-Madison, 1415 Engineering Dr, Madison, WI 53706

²Computing and Computational Sciences Directorate

Oak Ridge National Laboratory, P.O. Box 2008, Oak Ridge, TN 37831

³Mathematics and Computer Science Division

Argonne National Laboratory, Lemont, IL 60439

Abstract

Graph Neural Networks (GNNs) have emerged as a prominent class of data-driven methods for molecular property prediction. However, a key limitation of typical GNN models is their inability to quantify uncertainties in the predictions. This capability is crucial for ensuring the trustworthy use and deployment of models in downstream tasks. To that end, we introduce `AutoGNNUQ`, an automated uncertainty quantification (UQ) approach for molecular property prediction. `AutoGNNUQ` leverages architecture search to generate an ensemble of high-performing GNNs, enabling the estimation of predictive uncertainties. Our approach employs variance decomposition to separate data (aleatoric) and model (epistemic) uncertainties, providing valuable insights for reducing them. In our computational experiments, we demonstrate that `AutoGNNUQ` outperforms existing UQ methods in terms of both prediction accuracy and UQ performance on multiple benchmark datasets. Additionally, we utilize t-SNE visualization to explore correlations between molecular features and uncertainty, offering insight for dataset improvement. `AutoGNNUQ` has broad applicability in domains such as drug discovery and materials science, where accurate uncertainty quantification is crucial for decision-making.

Keywords: uncertainty quantification; graph neural networks; molecular property prediction; neural architecture search

1 Introduction

With the advancement of modern chemical synthesis platforms, the discovery of new molecules has become more efficient and data-driven models have become increasingly crucial for their generation

*Corresponding Author: sjiang87@wisc.edu

and evaluation. Among these models, Quantitative Structure-Activity Relationships (QSARs) are an established approach to predict molecular properties that would otherwise require expensive and time-consuming experimentation to be obtained. However, the prediction accuracy of QSARs is limited, and their applicability can be hindered by the requirement for pre-defined structural features [5]. In recent years, neural networks (NNs) have been increasingly employed for molecular property prediction, offering a more flexible alternative to traditional QSARs [41]. Unlike QSARs, NNs can learn complex, data-driven representations of molecules tailored to specific tasks, without relying on pre-defined molecular features designated by experts [9, 18, 14]. However, the use of NNs in molecular modeling still has limitations, particularly in terms of expressiveness and transparency. The complexity of NN models can make it difficult to assess their robustness, out-of-domain applicability, and potential failure modes.

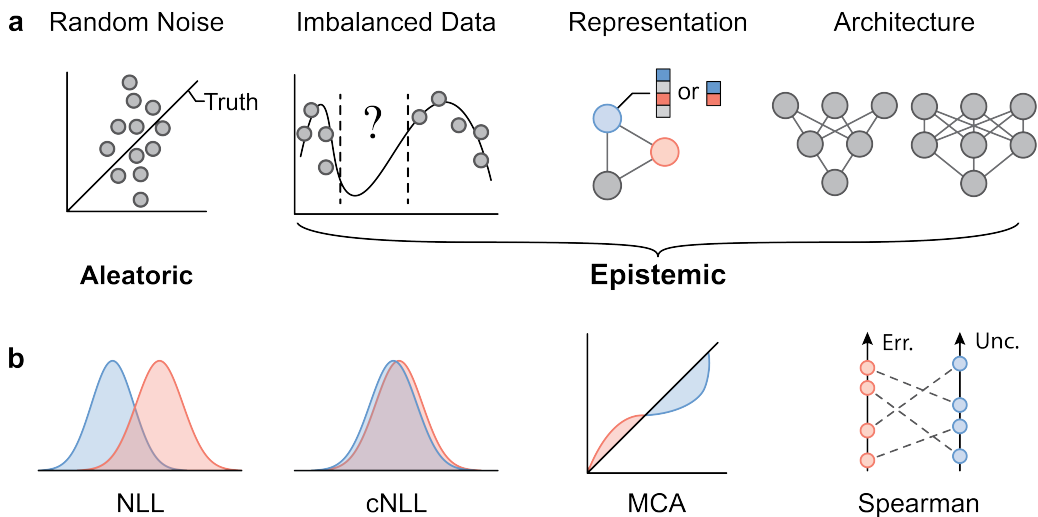


Figure 1: Sources of aleatoric and epistemic uncertainties and key metrics for quantifying uncertainty. (a) Aleatoric uncertainties arise from random noise in observations or measurements, while epistemic uncertainties arise from lack of information, such as imbalanced data, insufficient representation, and poor model architectures. (b) Common UQ metrics include negative log likelihood (NLL), calibrated NLL, miscalibration area (MCA), and Spearman’s rank correlation coefficient.

Incorporating uncertainty quantification (UQ) capabilities is essential to overcome the limitations of NNs in molecular modeling [11]. UQ refers to a set of mathematical techniques designed to quantify both aleatoric (or data) uncertainty and epistemic (or model) uncertainty. Aleatoric uncertainties arise from random noise in data observations or measurements and epistemic uncertainties arise from lack of knowledge, such as imbalanced data, insufficient data representation, or poor model architecture, as shown in Figure 1a. While aleatoric uncertainty is typically considered to be irreducible, epistemic uncertainty can be reduced (e.g., by collecting additional training data in relevant regions of an experimental space) [11]. By incorporating UQ techniques into NNs, valuable insights can be gained into the robustness and reliability of predictions, particularly in situations where data may be limited or noisy [35]. This is especially critical in molecular property predictions, where inaccurate predictions can have severe consequences. For example, a mispredicted toxicology profile of a drug

candidate could result in costly clinical trials being terminated or can even lead to a product recall [28]. By quantifying uncertainties associated with molecular property predictions, UQ can help identify potential sources of error, enhance model transparency, and ultimately enable the development of more accurate and reliable models [35]. Moreover, data accessibility issues often necessitate the quantification of different uncertainty sources. Employing UQ can facilitate an understanding of the cost-benefit ratio of gathering new data, which is beneficial when it decreases epistemic uncertainties. However, if the prevailing uncertainties are aleatoric, which are inherently irreducible, the pursuit of new data may be unproductive.

In recent years, significant effort has been devoted to developing UQ techniques for NN models in molecular prediction. Gawlikowski et. al. have provided a comprehensive review of most UQ techniques [13], while Hirschfeld et. al. have applied multiple UQ techniques in molecular property prediction using graph NNs [20]. Various UQ techniques are often used, as summarized in Figure 2. Mean-variance estimation [33] is a popular method for quantifying uncertainty in machine learning models; in this method, the mean (μ) and variance (σ^2) of the model predictions are calculated over a set of inputs by assuming Gaussian noise associated with the prediction. The mean value represents the model best estimate of the predicted output, while the variance represents the uncertainty associated with that estimate.

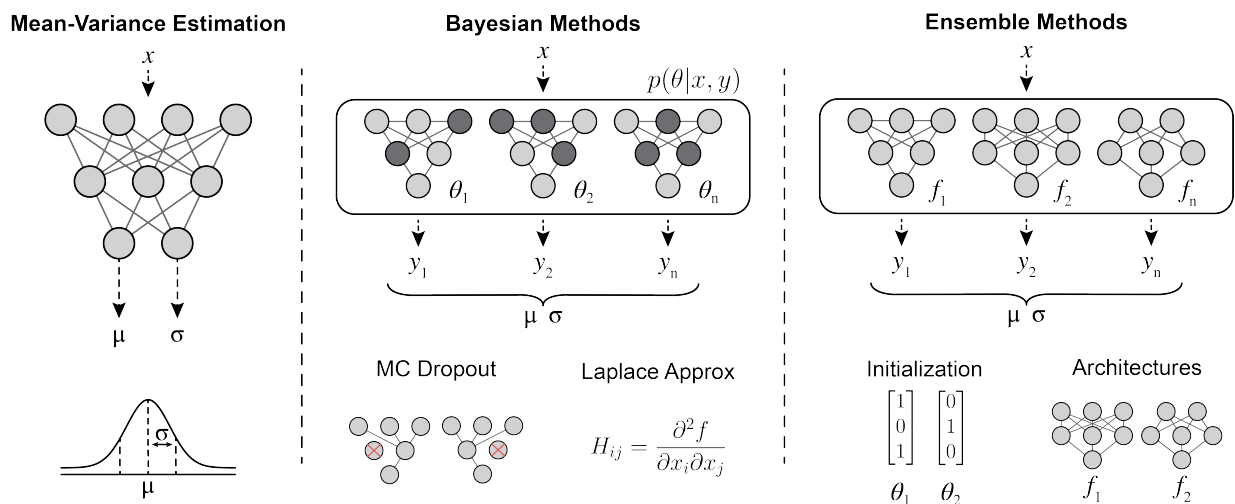


Figure 2: Various uncertainty quantification methods for neural networks.

Bayesian methods, another key paradigm of UQ, offer a probabilistic approach to modeling uncertainty in NNs. Monte Carlo dropout [10, 11, 12] is a widely used Bayesian method based on variational inference. This method involves randomly dropping out a proportion of the neurons during training and running multiple forward passes with different dropout masks to generate a distribution of predictions. Although Monte Carlo dropout has been shown to be effective in capturing model uncertainty and providing reliable uncertainty estimates [11], it is limited by the training conditions of the original model, which can lead to highly correlated predictions across models [21].

The so-called Laplace Approximation is another commonly used Bayesian UQ method that involves approximating the posterior distribution of NN parameters around a local mode of the loss

surface using a multivariate Gaussian distribution. The estimation of the Hessian matrix of the NN is critical to the Laplace Approximation, but this typically cannot be directly computed due to the massive number of parameters involved. Therefore, several techniques have been proposed, such as layer-wise Kronecker Factor approximation [16, 37]. While the Laplace Approximation requires only one NN model (thus being efficient) [26], it has some limitations. For example, it assumes that the posterior distribution is approximately Gaussian, which may not hold true far from the mode. Additionally, the Laplace Approximation involves fidelity-complexity trade-offs and can be sensitive to the training conditions.

Ensemble methods are also widely used for UQ and involve the aggregation of predictions from multiple models, referred to as ensemble members, to derive a final prediction. This approach aims to enhance generalization by leveraging the complementary strengths of the individual models [17]. To maximize the diversity among the individual models, various techniques have been explored, including distinct random initialization of models [25], Bagging and Boosting [27], and ensembling of different network architectures [19, 8]. Egele et al. recently demonstrated that the use of diverse network architectures can significantly increase the diversity within the ensemble, thereby leading to more accurate estimates of model uncertainty [8]. Moreover, they introduced a novel strategy for training multiple candidate models in parallel, which greatly reduces computational time. Ensemble methods have shown to be effective in achieving reliable uncertainty estimates and are easy to apply and parallelize, making them a practical choice for UQ applications.

Despite recent progress in UQ for NNs, several challenges remain to be addressed. One of the most significant challenges is the need to separate aleatoric and epistemic uncertainty. This separation is crucial, as it enables us to understand the sources of uncertainty in the model and provides insight into how we can improve it. For instance, quantifying epistemic uncertainty can inform the need to collect more data or improve the model architecture, such as incorporating additional features or using a more complex NN. Moreover, the accuracy of the model prediction is fundamental to the quality of UQ. Without an accurate model prediction, the UQ output will be unreliable and potentially misleading.

To address these challenges, this paper proposes an approach, which we call `AutoGNNUQ`, for constructing a diverse ensemble of GNN models for molecular property prediction by adapting the `AutoDEUQ` method [8]. `AutoGNNUQ` employs an aging evolution (AE) [36] approach to search for network architectures, with each model trained to minimize the negative log likelihood to capture aleatoric uncertainty. The approach then selects a set of models from the search to construct the ensembles and model epistemic uncertainty without sacrificing the quality of aleatoric uncertainty. The method achieves high prediction accuracy and UQ performance on several benchmark datasets, outperforming existing algorithms. Moreover, the decomposition of aleatoric and epistemic uncertainty provides insights into possible areas for reducing uncertainty. The proposed approach has the potential to significantly enhance UQ techniques for GNN models in molecular prediction, leading to more reliable and efficient active learning and experimental design. We provide extensive benchmark results against established UQ paradigms and datasets to demonstrate the benefits of the proposed approach. We provide all data and code needed for implementing our approach and for reproducing the benchmark results.

2 Methods

The AutoGNNUQ workflow, illustrated in Figure 3, consists of three key steps which we will detail in this section. First, molecular data are represented as graphs with atomic and bond features. Second, a neural architecture search (NAS) algorithm is employed to identify high-performing GNN models for UQ. Third, a diverse ensemble of these high-performing models is assembled, resulting in accurate molecular property prediction, high UQ performance, and decomposition of total uncertainty into aleatoric and epistemic uncertainties.

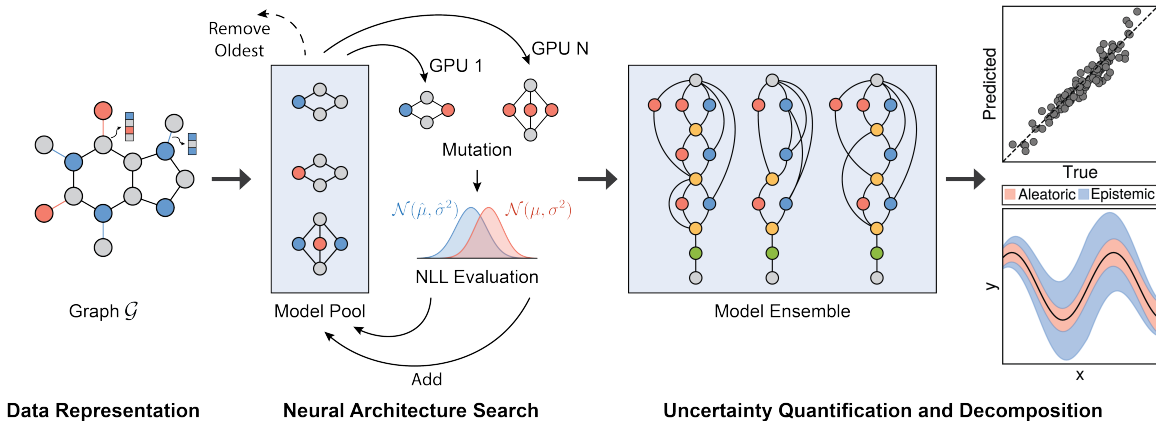


Figure 3: Workflow of AutoGNNUQ for uncertainty quantification in molecular property prediction. A molecular structure is represented as a graph with node features representing atoms and edge features representing bonds. Graph neural networks are used for uncertainty quantification (UQ). To optimize UQ performance, a neural architecture search algorithm using aging algorithms continuously mutates the architecture and evaluates UQ performance using the negative log likelihood loss function. The resulting high-performing models are added to a model pool, and the oldest models are removed. From this pool, an ensemble of models is selected to achieve high molecular property prediction accuracy and UQ performance as well as to decompose aleatoric and epistemic uncertainties.

2.1 Dataset and Representation

We evaluated the efficacy of the proposed AutoGNNUQ approach for molecular property prediction and UQ using four benchmark datasets from MoleculeNet [42]. These datasets were also employed in the previous UQ benchmark study [20]. The Lipo dataset [30] contains 4,306 compounds with measured octanol-water partition coefficients (logP). It aims to predict the lipophilicity of compounds, which is an essential property in drug discovery as it influences drug absorption, distribution, and metabolism within the human body. The FreeSolv dataset [31] comprises 643 small molecules with the solvation free energy as a thermodynamic quantity that characterizes the interaction between a solute and solvent. The ESOL dataset [6] includes 1,128 compounds with measured solubility in water ranging from 0.001 to 10,000 mg/L. Finally, the QM7 dataset [3, 32] contains atomization energies of 7,211 organic molecules with up to seven heavy atoms (*i.e.*, C, N, O, and S).

For consistency with prior research, we utilized identical graph representations of molecules where atoms serve as nodes and bonds as edges. Additionally, we adopted the same features used in the benchmark investigation [20], which consist of 133 atomic features and 14 bond features. The atomic features encompass several characteristics such as atomic number, degree, formal charge, chirality, number of hydrogens, and types of hybridization. The bond features, on the other hand, capture properties such as bond type, chirality, whether it is conjugated, and whether it is in a ring.

2.2 Neural Architecture Search and Ensemble Construction

The AutoGNNUQ NAS process consists of two main components, which are detailed below. First, a search space is established that comprises a range of feasible architectures using a message passing neural network (MPNN), a type of GNN, for extracting molecular features. Second, a search method is employed to explore this search space and identify the high-performing MPNN architecture for UQ. To generate a catalog of NNs, we execute AutoGNNUQ and store all models from the runs. To construct an ensemble \mathcal{E} of models from the model pool \mathcal{C} , we use a top-K approach, selecting the top K architectures with the lowest validation loss (*i.e.*, negative log likelihood). Specifically, we set K to 10 to ensure sufficient diversity and model representation in the ensemble.

2.2.1 Search Space

We have defined the AutoGNNUQ search space as a directed acyclic graph, illustrated in Fig. 4. The search space has fixed input and output nodes denoted by \mathcal{I} and \mathcal{O} , respectively. All other nodes, denoted by \mathcal{N} , represent intermediate nodes and contain a list of feasible operations. These intermediate nodes can be categorized into two types: constant nodes that contain a single operation, and variable nodes that contain multiple operations. For each variable node, an index is assigned to each operation. An architecture in the search space can be defined using a vector $\mathbf{p} \in \mathbb{Z}^n$, where n is the number of variable nodes. Each entry \mathbf{p}_i represents an index chosen from a set of feasible index values for the variable node i . The AutoGNNUQ search space is composed of MPNN, skip-connection, and gather variable nodes, which are further elaborated below.

1. **Input node.** The input node consists of several components, including node features, edge features, edge pairs, and node masks. To construct the feature matrices for a given dataset of molecules, we consider the maximum number of nodes and edges as N and E , respectively. We pad the node feature matrix with zeros to generate $\mathbf{H} \in \mathbb{R}^{N \times F_n}$, and the edge feature matrix with zeros to generate $\mathbf{E} \in \mathbb{R}^{E \times F_e}$, where F_n and F_e represent the number of node features and edge features, respectively. Additionally, we employ an edge pair matrix $\mathbf{P} \in \mathbb{Z}^{E \times 2}$, where each row denotes the indices of two nodes connected by an edge. Given that molecules can have different numbers of nodes, we use a node mask vector $\mathbf{m} \in \mathbb{Z}^N$ to exclude non-existent node features that occur from zero padding. A present node is denoted by $\mathbf{m}_i = 1$, while a non-existent node is indicated by $\mathbf{m}_i = 0$.
2. **MPNN node.** The MPNN node updates the hidden features of each node for T time steps using

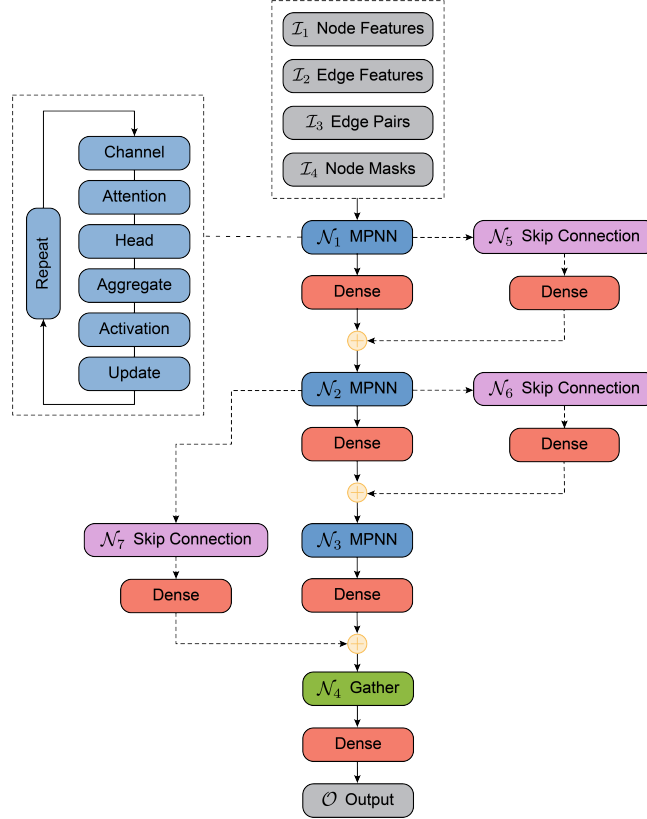


Figure 4: Example `AutoGNNUQ` search space with three MPNN variable nodes in blue (\mathcal{N}_1 , \mathcal{N}_2 , and \mathcal{N}_3), skip-connection variable nodes in pink (\mathcal{N}_5 , \mathcal{N}_6 , and \mathcal{N}_7), and a gather variable node in green (\mathcal{N}_4). Dotted lines represent possible skip connections. The MPNN takes as input node features (\mathcal{I}_1), edge features (\mathcal{I}_2), edge pairs (\mathcal{I}_3), and node masks (\mathcal{I}_4), and consists of two constant dense nodes with 32 hidden units before outputting a single node (\mathcal{O}). The MPNN node includes several variables such as the number of channels, attention mechanisms, number of attention heads, aggregation methods, activation functions, update functions, and number of repetitions.

a message function M_t and an update function U_t . These functions are defined as follows:

$$\mathbf{m}_v^{t+1} = \text{Agg}_{w \in \mathcal{N}(v)} M_t(\mathbf{h}_v^t, \mathbf{h}_w^t, \mathbf{e}_{vw}) \quad (1a)$$

$$\mathbf{h}_v^{t+1} = U_t(\mathbf{h}_v^t, \mathbf{m}_v^{t+1}). \quad (1b)$$

To update the hidden feature of a node v at step t , the message function M_t takes as inputs the node v feature \mathbf{h}_v^t , the neighboring node features \mathbf{h}_w^t for $w \in \mathcal{N}(v)$, and the edge feature \mathbf{e}_{vw} between node v and w . The output of the message function M_t is a list of message vectors from neighboring nodes, which are collected and used by the aggregate function Agg to generate the intermediate hidden feature \mathbf{w}_v^{t+1} . The aggregate function can be one of mean, summation or max pooling. At each step t , the update function U_t merges the node feature \mathbf{h}_v^t with the intermediate hidden feature \mathbf{m}_v^{t+1} to generate the new hidden feature \mathbf{h}_v^{t+1} for the next step $t + 1$. The message function M_t and update function U_t are described in detail as follows:

$$M_t(\mathbf{h}_v^t, \mathbf{h}_w^t, \mathbf{e}_{vw}) = \alpha_{vw} \text{MLP}(\mathbf{e}_{vw}) \mathbf{h}_w^t \quad (2a)$$

$$U_t(\mathbf{h}_v^t, \mathbf{m}_v^{t+1}) = \begin{cases} \text{GRU}(\mathbf{h}_v^t, \mathbf{m}_v^{t+1}) \\ \text{MLP}(\mathbf{h}_v^t, \mathbf{m}_v^{t+1}) \end{cases}. \quad (2b)$$

The message function involves a multilayer perceptron (MLP), also known as an edge network, to manage the edge feature \mathbf{e}_{vw} . After being processed by the MLP, the edge feature is multiplied by \mathbf{h}_w^t to produce a message from node w to v . In this situation, the processed edge feature $\text{MLP}(\mathbf{e}_{vw})$ can be considered as a weight for \mathbf{h}_w^t . Building on the concept of node attention, we introduce an attention coefficient α_{vw} to adjust the weight of \mathbf{h}_w^t . This coefficient is determined by a function of both \mathbf{h}_v^t and \mathbf{h}_w^t . The update function U_t can either be a gated recurrent unit (GRU) or a multilayer perceptron (MLP). To provide additional clarity regarding the design of the MPNN node, we can break it down into the following five operational categories.

- (a) **Hidden dimension.** After T iterations, the MPNN node transforms the input node feature into a d -dimensional vector. The selection of the hidden dimension d plays an important role in the prediction. In order to enhance generalization and reduce the number of parameters, we select the set of state dimensions to $\{8, 16, 32, 64\}$.
- (b) **Attention function.** While conventional MPNNs rely on the edge feature to dictate the weight of information propagation between nodes, the attention mechanism enables prioritization of the most pertinent neighboring nodes, thereby improving the process of information aggregation. Drawing upon our prior research [23], we employ a range of attention functions including Constant, GAT, SYM-GAT, COS, Linear, and Gen-linear (see details in SI).
- (c) **Attention head.** The use of multihead attention can be advantageous in ensuring stable learning [40]. We select the number of heads from the set of $\{1, 2, 3\}$.
- (d) **Aggregate function.** The selection of an appropriate aggregation function is crucial in capturing neighborhood structures and extracting node representation [43]. We choose our aggregation functions from the set of $\{\text{mean, summation, max-pooling}\}$.

- (e) **Activation function.** As per our prior research [23], we consider a range of activation functions {Sigmoid, Tanh, ReLU, Linear, Softplus, LeakyReLU, ReLU6, and ELU}.
 - (f) **Update function.** Combining node features \mathbf{h}_v^t with intermediate hidden features \mathbf{m}_v^{t+1} and propagating them using an update function enables the generation of new features, denoted as \mathbf{h}_v^{t+1} . Our update functions are chosen from the set {GRU, MLP}.
3. **Skip-connection node.** The skip-connection node is a type of variable node that enables a connection between nodes \mathcal{N}_{i-1} , \mathcal{N}_i , and \mathcal{N}_{i+1} in a sequence. The purpose of the skip-connection is to add or skip a node within a sequence. This operation involves two possible actions: identity for skip-connection or empty for no skip-connection. In a skip-connection operation, the tensor output from \mathcal{N}_{i-1} is processed by a dense layer, which ensures the incoming tensor is projected to the appropriate shape for summation. The summation operator is then applied to add the output from \mathcal{N}_{i-1} and \mathcal{N}_i , producing a result that is passed to \mathcal{N}_{i+1} . The skip-connection can be applied to any length of node sequences, but in this study, it is limited to a maximum of three nodes to restrict complexity. For instance, \mathcal{N}_{i-1} may be added to \mathcal{N}_{i+2} and passed to \mathcal{N}_{i+3} .
 4. **Gather variable node.** The gather node consists of eleven operations categorized into five different types. The input to the gather node is the node feature matrix $\mathbf{H} \in \mathbb{R}^{N \times F}$, where N represents the number of nodes and F represents the number of hidden features. The graph operations used in the AutoGNNUs can be segregated into five categories based on the gather operations provided in the Spektral GNN package [15].
 - (a) **Global pool.** Aggregate node features through the computation of the sum, mean, or maximum. The output has a shape represented by \mathbb{R}^N .
 - (b) **Global gather.** Compute the sum, mean, or maximum of a feature for all the nodes. The output has a shape of \mathbb{R}^F .
 - (c) **Global attention pool.** Calculate the output $\mathbf{H}_{out} \in \mathbb{R}^{F'}$ as $\mathbf{H}_{out} = \sum_{i=1}^N (\sigma(\mathbf{H}\mathbf{W}_1 + \mathbf{b}_1) \odot (\mathbf{H}\mathbf{W}_2 + \mathbf{b}_2))_i$. Here, σ represents the sigmoid activation function, and \mathbf{W}_1 and \mathbf{W}_2 represent trainable weights, while \mathbf{b}_1 and \mathbf{b}_2 represent biases. The output dimension F' can be selected from the set {16, 32, 64}.
 - (d) **Global attention sum pool.** Aggregate a graph by learning attention coefficients to sum node features. The operation can be defined as follows: $\mathbf{H}_{out} = \sum_{i=1}^N \alpha_i \mathbf{H}_i$, where α is defined as $\text{softmax}(\mathbf{H}\mathbf{a})$, and \mathbf{a} is a trainable vector. The softmax activation is applied across all the nodes.
 - (e) **Flatten.** Flatten \mathbf{H} into a 1D vector.

The total number of possible architectures in the search space is 29,059,882,942,464 ($\approx 2 \times 10^{13}$). This highlights the rich model space that the proposed AutoGNNUs approach has available.

2.2.2 Search Method

In order to discover high-performing neural architectures from the search space, we use the aging evolution (AE) method [36], which is an asynchronous search technique that is available in the

DeepHyper package [2]. The AE algorithm starts with a population of P random architectures, evaluates them, and records the validation loss of each one. After the initialization, the algorithm samples N random architectures uniformly from the population, and the architecture with the lowest validation loss in the sample is chosen as the parent. A mutation is then applied to the parent, which corresponds to selecting a different operation for a variable node in the search space. This creates a new child architecture that is trained, and its validation loss is recorded. The child architecture is added to the population by replacing the oldest architecture in the population. Over multiple cycles, the algorithm retains architectures with lower validation loss via repeated sampling and mutation. AE is highly scalable as it can leverage multiple compute nodes to evaluate architectures in parallel, resulting in faster convergence to high-performing architectures. AE has been shown to outperform reinforcement learning methods for NAS due to its minimal algorithmic overhead and synchronization [29, 36].

2.2.3 Search Process

We adopt the same approach for splitting the data as the benchmark study [20] to ensure consistency and comparability. We use the identical 8 random seeds as used in [20] for partitioning the data into training, validation, and testing sets. The data is divided into training, validation, and testing sets with a ratio of 5:2:3, respectively. The training set is utilized to optimize the model parameters, while the validation set guides the NAS. Finally, the performance of the model is evaluated using the testing set. During the search process, we imposed a time limit on the training for each architecture, limiting all datasets to 30 epochs. For QM7, the batch size was set to 50, while for the other datasets it was set to 200. We utilized the Adam [24] optimizer with a learning rate of 0.001 and performed 500 architecture searches. Once the search was complete, we performed post-training by selecting 10 architectures with the lowest validation loss and training them from scratch for 200 epochs to form the ensemble \mathcal{E} .

2.3 Uncertainty Quantification and Decomposition

The dataset, denoted by \mathcal{D} , comprises input graphs $\mathbf{x} \in \mathcal{X}$ and their corresponding outputs $y \in \mathcal{Y}$, where \mathcal{X} and \mathcal{Y} represent the input and output spaces, respectively. We focus on regression problems in which the output is a scalar or vector of real values. Our objective is to model the probabilistic predictive distribution $p(y|\mathbf{x})$ using a parameterized distribution $p_{\theta}(y|\mathbf{x})$, which estimates aleatoric uncertainty. To capture epistemic uncertainty, we use an ensemble of neural networks denoted by $p_{\mathcal{E}}(y|\mathbf{x})$, where \mathcal{E} represents the set of all models in the ensemble. The sample space for θ is defined as Θ , which represents the space of all possible values for the parameters in the parameterized distribution. By combining both aleatoric and epistemic uncertainties, we aim to improve the overall predictive performance and UQ in molecular property prediction tasks.

2.3.1 Aleatoric Uncertainty

To model aleatoric uncertainty, we use the quantiles of the probability distribution p_θ , where θ is partitioned into architecture decision variables θ_a (representing the network topology parameters) and model weights θ_w . We assume a Gaussian distribution for p_θ , such that $p_\theta \sim \mathcal{N}(\mu_\theta, \sigma_\theta^2)$, and measure aleatoric uncertainty using variance, consistent with previous works [8, 25]. The NN is trained to output both the mean μ_θ and the variance σ_θ^2 (which is essentially mean-variance estimation). To obtain the optimal choice of θ_w given a fixed θ_a , we seek to maximize the likelihood of the real data \mathcal{D} . This is achieved by minimizing the negative log-likelihood loss function [25], which is given by:

$$\mathcal{L}(\mathcal{D}; \theta) = -\log p_\theta = \frac{1}{2|\mathcal{D}|} \sum_{\mathbf{x}, y \in \mathcal{D}} \log(2\pi) + \log(\sigma_\theta(\mathbf{x})^2) + \frac{(\mu_\theta(\mathbf{x}) - y)^2}{\sigma_\theta(\mathbf{x})^2}. \quad (3)$$

2.3.2 Epistemic Uncertainty

To account for epistemic uncertainty, we employ ensembles consisting of multiple neural networks (NNs) [25]. Our approach involves generating a collection of NNs, denoted by $\mathcal{C} = \theta_i, i = 1, 2, \dots, c$, where each θ is a combination of architecture decision variables and model weights. We then select K models from this collection to form the ensemble, where $\mathcal{E} = \theta_i, i = 1, 2, \dots, K$ and K denotes the ensemble size.

To describe the probability of $\theta \in \mathcal{E}$, we define a probability measure $p : \Theta \rightarrow [0, 1] \in \mathbb{R}$ such that $p(\theta)$ represents the probability of θ being present in the ensemble. To obtain the overall probability density function of the ensemble and effectively model epistemic uncertainty, we use a mixture distribution, which is a weighted average of the probability density functions of all the members in the ensemble. Specifically, we have:

$$p_\mathcal{E} = \mathbb{E}_{\theta \sim p(\mathcal{E})} p_\theta, \quad (4)$$

where p_θ represents the parameterized distribution that estimates the probabilistic predictive distribution $p(y|\mathbf{x})$ for a given θ , and $p(\mathcal{E})$ refers to a probability distribution over the ensemble. This approach allows us to effectively model epistemic uncertainty by capturing the diversity of predictions made by different NNs in the ensemble.

2.3.3 Uncertainty Decomposition

By the law of total variance [8], we have that

$$\mu_\mathcal{E} := \mathbb{E}_{\theta \sim p(\mathcal{E})} [\mu_\theta] \quad (5a)$$

$$\begin{aligned} \sigma_\mathcal{E}^2 &:= \mathbb{V}_{\theta \sim p(\mathcal{E})} [p_\mathcal{E}] \\ &= \underbrace{\mathbb{E}_{\theta \sim p(\mathcal{E})} [\sigma_\theta^2]}_{\text{Aleatoric Uncertainty}} + \underbrace{\mathbb{V}_{\theta \sim p(\mathcal{E})} [\mu_\theta]}_{\text{Epistemic Uncertainty}}, \end{aligned} \quad (5b)$$

where \mathbb{E} refers to the expected value and \mathbb{V} refers to the variance.

Eq. 5b provides a formal decomposition of the overall uncertainty of the ensemble into its individual components such that

- $\mathbb{E}_{\theta \sim p(\mathcal{E})}[\sigma_{\theta}^2]$ marginalizes the effect of θ and characterizes the aleatoric uncertainty.
- $\mathbb{V}_{\theta \sim p(\mathcal{E})}[\mu_{\theta}]$ captures the spread of the prediction across different models and ignores the noise present in the data, therefore characterizing the epistemic uncertainty.

If we assume that $p(\mathcal{E})$ is uniform in the mixture distribution, meaning that the weights are equal, we can calculate the two values in Eq. 5b using empirical mean and variance estimates,

$$\mu_{\mathcal{E}} = \frac{1}{K} \sum_{\theta \in \mathcal{E}} \mu_{\theta} \quad (6a)$$

$$\sigma_{\mathcal{E}}^2 = \underbrace{\frac{1}{K} \sum_{\theta \in \mathcal{E}} \sigma_{\theta}^2}_{\text{Aleatoric Uncertainty}} + \underbrace{\frac{1}{K-1} \sum_{\theta \in \mathcal{E}} (\mu_{\theta} - \mu_{\mathcal{E}})^2}_{\text{Epistemic Uncertainty}} \quad (6b)$$

where K is the size of the ensemble.

In this context, we have established that the overall uncertainty σ^2 is the sum of two distinct sources, namely the aleatoric and epistemic uncertainty. The aleatoric uncertainty is determined by the mean value of the predictive variance of each model in the ensemble, whereas the epistemic uncertainty is determined by the predictive variance of the mean value of each model in the ensemble.

2.4 Evaluation Metrics

To evaluate the performance of different UQ strategies, we employ the following metrics.

2.4.1 Negative Log Likelihood (NLL)

One of the primary metrics used in our benchmark study is the negative log likelihood (NLL), which quantifies the likelihood of the observed errors under the assumption that they follow a normal distribution with variances derived from the UQ estimates, denoted as $\sigma(\mathbf{x})^2$ [25]. The NLL is calculated by taking the average of the negative logarithm of the likelihood function across all test molecules, and can be expressed as:

$$\text{NLL}(\mathcal{D}_{\text{test}}) = \frac{1}{2|\mathcal{D}_{\text{test}}|} \sum_{\mathbf{x}, y \in \mathcal{D}_{\text{test}}} \log(2\pi) + \log(\sigma(\mathbf{x})^2) + \frac{(\mu(\mathbf{x}) - y)^2}{\sigma(\mathbf{x})^2} \quad (7)$$

where $\mu(\mathbf{x})$ is the model prediction and $\sigma(\mathbf{x})^2$ is the UQ estimate for molecule \mathbf{x} .

2.4.2 Calibrated NLL

The uncalibrated NLL metric solely captures the difference between the predicted and true probability distributions. For reliable estimation of uncertainty, the predicted probabilities must be calibrated to match the true probabilities. Instead of considering the true variance as $\sigma(\mathbf{x})^2$, it is instead assumed to be linearly correlated as $a\sigma(\mathbf{x})^2 + b$ [22].

The calibrated NLL (cNLL) is determined for each dataset and method by minimizing the NLL in the validation set through the selection of scalars a and b .

$$\text{cNLL} = \frac{1}{2|\mathcal{D}_{\text{test}}|} \frac{1}{2|\mathcal{D}_{\text{test}}|} \sum_{\mathbf{x}, y \in \mathcal{D}_{\text{test}}} \log(2\pi) + \log(a_*\sigma(\mathbf{x})^2 + b_*) + \frac{(\mu(\mathbf{x}) - y)^2}{a_*\sigma(\mathbf{x})^2 + b_*} \quad (8a)$$

$$(a_*, b_*) = \underset{\mathbf{x}, y \in \mathcal{D}_{\text{val}}}{\text{argmin}} \log(2\pi) + \log(a\sigma(\mathbf{x})^2 + b) + \frac{(\mu(\mathbf{x}) - y)^2}{a\sigma(\mathbf{x})^2 + b} \quad (8b)$$

2.4.3 Miscalibration Area

The proper calibration of UQ models is crucial for their reliable application in decision-making processes. A well-calibrated model can be evaluated through the miscalibration area, which quantifies the extent of the discrepancy between the predicted and actual uncertainties. This area can be calculated by comparing the frequency distribution of the predicted uncertainties with the observed uncertainties. A small miscalibration area indicates that the model predicted uncertainty aligns with the real-world uncertainty, while a large miscalibration area implies a poorly calibrated model.

Tran et al. [38] propose a novel method to assess the calibration of UQ models. This method compares the observed fraction of errors falling within z standard deviations of the mean to the expected fraction for a Gaussian random variable with variance equal to the uncertainty prediction $\sigma(\mathbf{x})^2$. By doing so, it can determine if a model is systematically overconfident or underconfident. A perfect UQ metric would have an area of zero, indicating a perfect match between the expected and observed fractions for any z . However, it is important to note that the miscalibration area only provides directional information about the model misprediction, rather than the degree of misprediction. Therefore, a model that is overconfident about some points and underconfident about others could still achieve a perfect score of 0.

2.5 Spearman’s Rank Correlation Coefficient

Spearman’s (rank correlation) coefficient is a useful tool in UQ for assessing the correlation between predicted uncertainties and actual errors. In any uncertainty estimator, we expect that predictions with lower uncertainty will be associated with lower true error. Specifically, if we have a model and two molecules \mathbf{a} and \mathbf{b} for which $\sigma_{\mathbf{a}}^2 < \sigma_{\mathbf{b}}^2$, we expect that $\mu\mathbf{a}$ will be more accurate on average than $\mu\mathbf{b}$.

To measure the correlation between an absolute error vector \mathbf{m} and a predicted uncertainty vector \mathbf{n} , we define rank vectors $r_{\mathbf{m}}$ and $r_{\mathbf{n}}$, which assign integer ranks to each value in ascending order. The correlation coefficient is then calculated based on the covariance (cov) and standard deviations σ of the rank vectors as

$$\rho(\mathbf{m}, \mathbf{n}) = \frac{\text{cov}(r_{\mathbf{m}}, r_{\mathbf{n}})}{\sigma(r_{\mathbf{m}})\sigma(r_{\mathbf{n}})}. \quad (9)$$

If \mathbf{m} and \mathbf{n} have the same ranking, $\rho(\mathbf{m}, \mathbf{n})$ is 1, and if \mathbf{m} and \mathbf{n} have opposite rankings, $\rho(\mathbf{m}, \mathbf{n})$ is -1 . However, it is important to note that we do not expect a perfect correlation of $\rho = 1$ since we assume that the errors will follow a normal distribution. Thus, it is possible for the model to occasionally produce a result with low error, even if it has high uncertainty.

2.6 Computational Resources

We used the Nightingale GPU cluster at the University of Wisconsin-Madison, consisting of a couple nodes, each of which was equipped with an RTX 6000 GPU having 24 GB GDDR memory. The software environment used in our experiment was based on Python 3.8 and TensorFlow 2.5.0 [1]. For neural architecture search, we used DeepHyper 0.3.3 [2], which employed the TensorFlow-Keras API. For analysis, we used RDKit 2021.03.5 and Scikit-learn 1.1.2 [34].

3 Benchmark Results

3.1 Neural Architecture Search

The efficient discovery of accurate molecular representations is crucial for advancing drug discovery and material design. In this work, we employed the AE search method, which executed 500 evaluations (small part of architecture space) to discover optimal architectures for predicting molecular properties. The search trajectory of the reward (log likelihood) with respect to the evaluations is presented in Figure 5, where a running average with a window size of 20 was applied to minimize noise and produce a smooth visualization of trends in the data. The solid line in the graphic represents the average reward accrued over eight different random seeds, with the shaded area denoting the standard deviation. We defined search convergence as the point where the reward trajectory reaches a plateau, as observed in Figure 5. On average, for all datasets, our analysis revealed that the AE convergence occurred after approximately 300 evaluations. Notably, in the case of ESOL, significant reward fluctuation was observed around the 150 and 300 evaluations mark. This variation is attributed to an unusually low reward value for a specific random seed 7, further illustrated in Figure S3-S10. Examples of the optimal and suboptimal architectures discovered during the search are presented in SI Figures S1 and S2, respectively.

As previously stated, accurate predictions are a critical element of effective UQ. The regression results of the AutoGNNUQ method, as presented in Figure 6, effectively showcase its performance across all eight random seed splits of the test dataset. All test set prediction points aligned close to the diagonal line, indicating that the predicted values of AutoGNNUQ are close to the true values. Although the QM7 parity plot illustrates a discernible spread of predictions, a substantial number of points still cluster near the diagonal line, leading to visual overlap. Specifically, as shown in Table 1, the MAE of AutoGNNUQ on QM7 is 48.1 ± 2.5 , which is a 38% drop from the MoleculeNet benchmark MAE of 77.9 ± 2.1 . The RMSE of AutoGNNUQ on Lipo is 0.656 ± 0.020 , which is 8% lower than the MoleculeNet result of 0.715 ± 0.035 . MoleculeNet displays a superior performance with a lower RMSE of 0.58 ± 0.03 on ESOL and 1.15 ± 0.12 on FreeSolv, in contrast to AutoGNNUQ’s RMSE values of 0.77 ± 0.13 and 1.26 ± 0.12 , respectively. Given the small size of the ESOL and FreeSolv test sets, consisting of only 339 and 193 molecules respectively, the results are susceptible to variations due to different random seeds used in MoleculeNet. Moreover, small datasets inherently tend to induce overfitting, potentially leading to suboptimal outcomes in AutoGNNUQ. Overall, AutoGNNUQ has achieved commendable prediction accuracy, which is the foundation of good UQ performance.

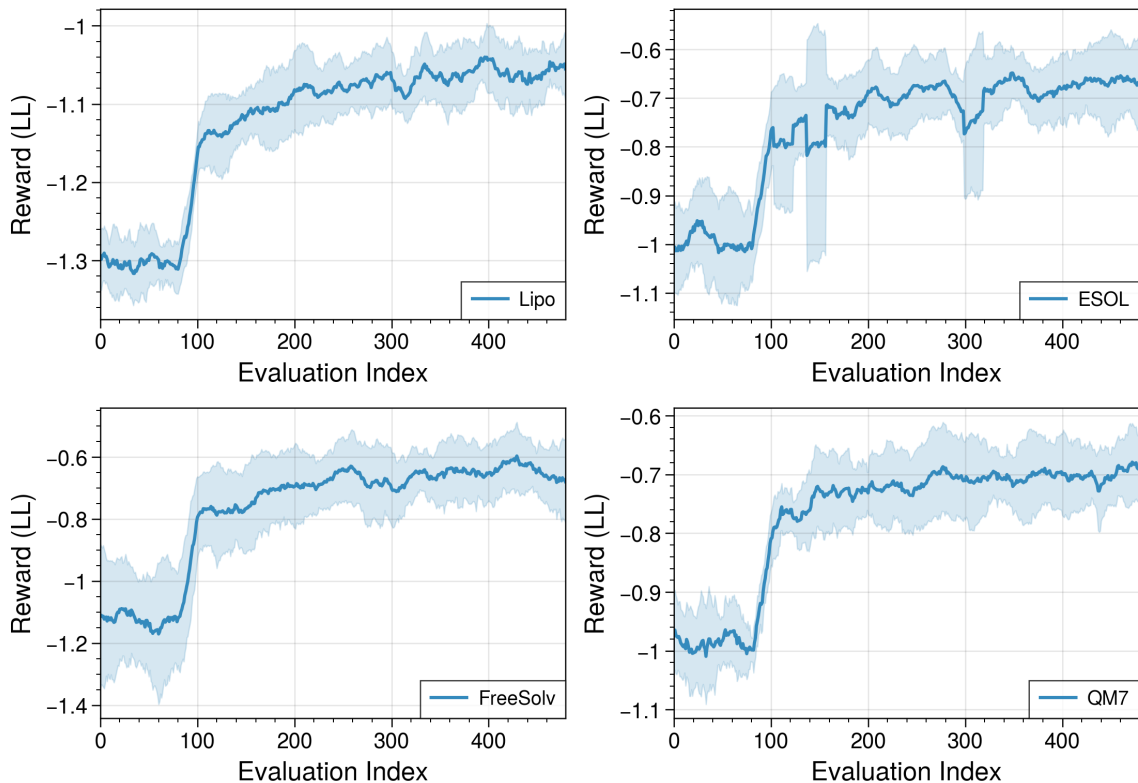


Figure 5: Search trajectories represented for all datasets across eight distinct random seeds. The solid line depicts the average reward while the shaded region indicates the standard deviation. Rewards for all datasets correspond to log-likelihood (LL) values, which we aim to maximize.

Table 1: Property prediction results as generated by the `AutoGNNuQ` and `MoleculeNet` benchmark. Values represent the mean across eight random seeds with corresponding standard deviations.

Dataset	AutoGNNuQ	MoleculeNet
Lipo (RMSE)	0.656 \pm 0.020	0.715 \pm 0.035
ESOL (RMSE)	0.77 \pm 0.13	0.58 \pm 0.03
FreeSolv (RMSE)	1.26 \pm 0.12	1.15 \pm 0.12
QM7 (MAE)	48.1 \pm 2.4	77.9 \pm 2.1

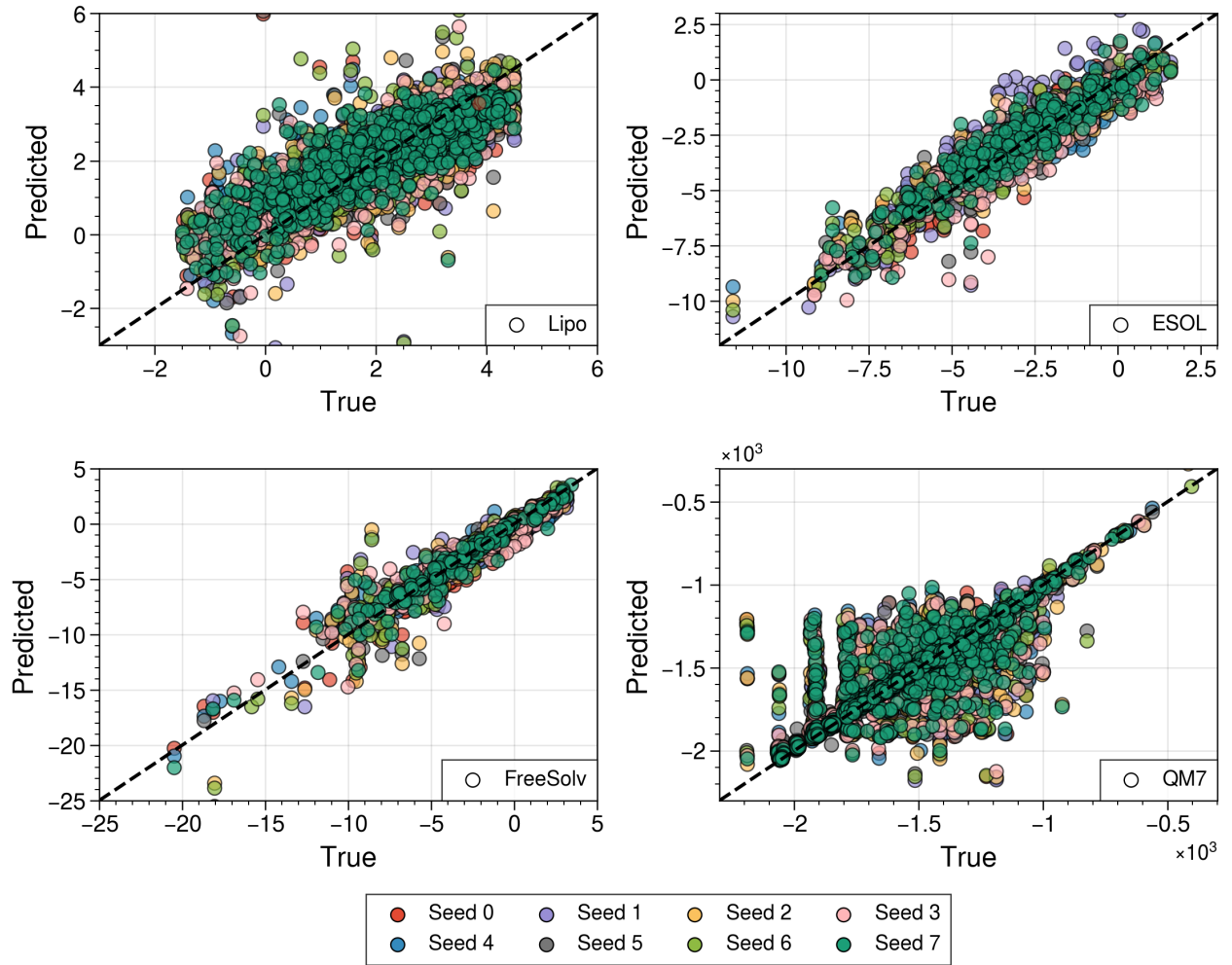


Figure 6: Parity plots of all test datasets derived from eight distinct random seeds. The diagonal line in each plot represents perfect prediction.

3.2 UQ performance

3.2.1 Negative Log Likelihood (NLL)

The results presented in Figure 7 provide a rigorous evaluation of the ability of the proposed method to accurately estimate variances of normally distributed errors through negative log likelihood (NLL), which measures the quality of a probabilistic model’s ability to predict the likelihood of observed data given a set of parameters [20]. In comparison to the benchmark MPNN ensemble, AutoGNNUQ demonstrated superior performance across all datasets with mean NLL values of 0.9737, 1.1032, 1.4496, and 5.6974 for Lipo, ESOL, FreeSolv, and QM7, respectively. These values represent 92.45%, 91.79%, 89.63%, and 69.40% decrease compared to benchmark results. The superior performance of AutoGNNUQ could be attributed to the fact that its architecture search process is explicitly optimized for NLL, allowing it to more effectively explore the space of possible architectures and identify those that perform well on the UQ task. Additionally, AutoGNNUQ NLL values showed much less variation across different random seeds, possibly due to the effectiveness of the search process in identifying high-performing architectures.

3.2.2 Calibrated NLL (cNLL)

Figure 7 also presents the calibrated negative log likelihoods (cNLL) for each dataset, where $\hat{\sigma}^2(\mathbf{x}) := a\sigma^2(\mathbf{x}) + b$ is optimized based on the validation data using eq. 8b. The calibration process aims to identify the best values of a and b that minimize the cNLL. The results indicate that, after calibration, the benchmark results showed a decrease in cNLL values, while the change in AutoGNNUQ cNLL values was not significant, suggesting that AutoGNNUQ is already well calibrated. Notably, AutoGNNUQ still outperformed the benchmark MPNN ensemble across all datasets, with mean cNLL values of 1.1357, 1.2193, 1.5533, and 5.6801 for Lipo, ESOL, FreeSolv, and QM7, respectively. These values represent a reduction of 12.45%, 8.54%, 10.19%, and 44.63% compared to the benchmark results.

3.2.3 Miscalibration Area

In Figure 7, the miscalibration calibration area is shown. It is worth noting that the miscalibration area measures the systematic over- or under-confidence in an aggregated, quantitative sense, rather than the absolute errors of individual compounds. A score of 0 indicates perfect alignment, while a score of 0.5 indicates maximum misalignment.

AutoGNNUQ outperformed the benchmark MPNN ensemble in most datasets, as evidenced by mean miscalibration area values of 0.0605, 0.0566, and 0.1064 for Lipo, ESOL, and FreeSolv, respectively. This represents an 83.10%, 82.98%, and 70.72% reduction compared to the benchmark results. However, it is important to note that AutoGNNUQ has a miscalibration area of 0.2715 for QM7, which is 10.52% higher than the benchmark result.

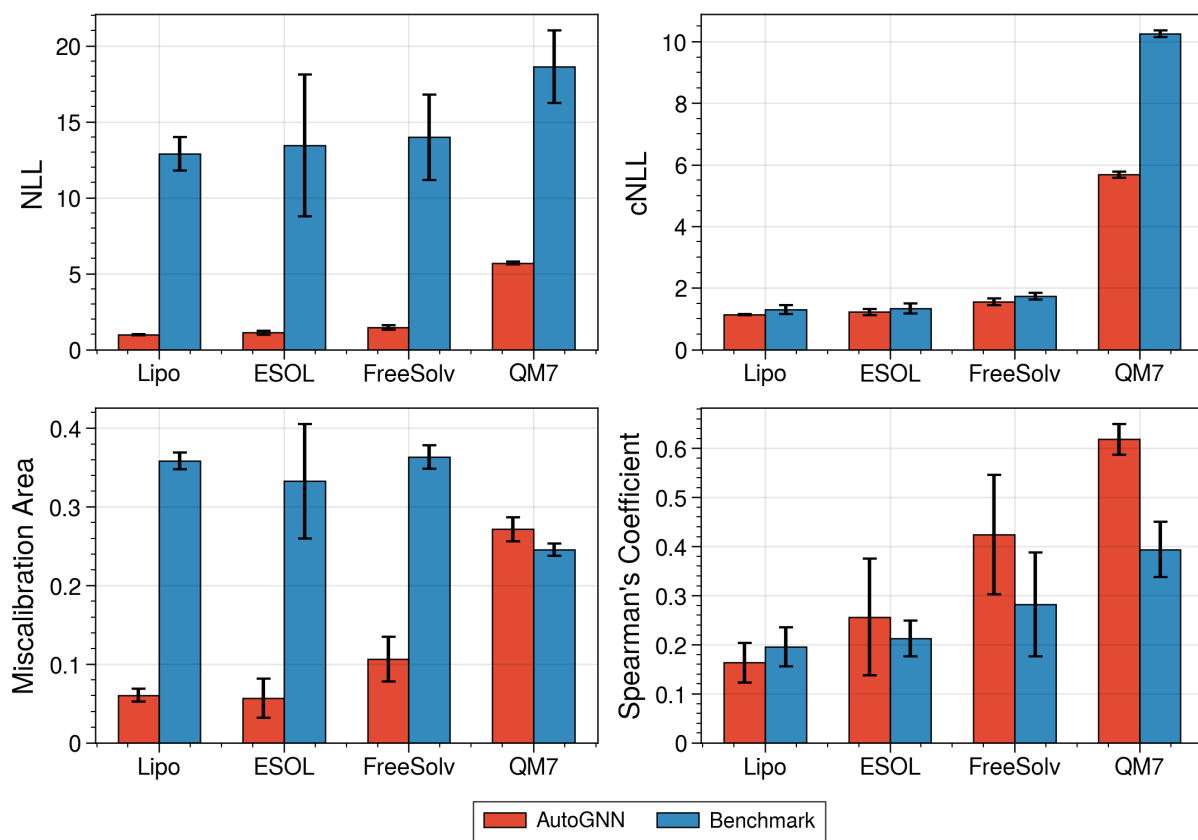


Figure 7: Comparison of `AutoGNN` and the benchmark model for UQ performance on all test datasets. The performance metrics evaluated include negative log-likelihood loss (NLL), calibrated NLL (cNLL), miscalibration area, and Spearman's coefficient. `AutoGNN` outperforms the benchmark model on NLL, calibrated NLL, and most datasets in terms of miscalibration area. The bars represent the mean values of the metrics over 8 different runs with different random seeds for test data splitting, while the error bars indicate the standard deviations.

3.2.4 Spearman’s Rank Correlation Coefficient

Figure 7 displays the Spearman’s rank correlation coefficient (Spearman’s coefficient), which indicates the relationship between uncertainty and prediction error. A score of 1 indicates a positive correlation between uncertainty and prediction error, while a score of -1 indicates a negative correlation, and a score of 0 indicates no correlation. For Lipo, AutoGNNUQ achieved coefficients of 0.1632, which is 16.52% lower than the benchmark result. For ESOL, FreeSolv and QM7, AutoGNNUQ achieved coefficients of 0.2563, 0.4240 and 0.6185, respectively, which are 20.49%, 50.24% and 57.02% higher than the benchmark result.

However, it is important to note that higher uncertainty values do not necessarily indicate high prediction error. A well-calibrated model that captures underlying noise in data can perform well despite high uncertainty. Moreover, limited data in certain input spaces can make it challenging to estimate the true level of uncertainty, leading to poor model performance despite low uncertainty and high error. Figure 8 illustrates that in many instances, high error is linked to low uncertainty, whereas low error is associated with high uncertainty.

3.3 Uncertainty Decomposition

The decomposition of uncertainty into aleatoric and epistemic uncertainties is a crucial aspect of statistical modeling and decision-making. As presented in Eq. 5b, aleatoric uncertainty is determined by the mean value of the predictive variance of each model in the ensemble, whereas epistemic uncertainty is determined by the predictive variance of the mean value of each model in the ensemble.

To illustrate this, Figure 9 displays the predicted value, aleatoric uncertainty, and epistemic uncertainty (represented by one standard deviation) based on the model architecture with the highest validation reward. The constant shaded regions in Lipo, ESOL, and FreeSolv datasets show a consistent level of uncertainty associated with each predicted value. However, QM7 exhibits fluctuations in the uncertainty values. Further visualized in Figure 10, the cumulative density distribution of aleatoric and epistemic uncertainties reveals that, in all datasets, epistemic uncertainty is smaller than aleatoric uncertainty, which is indicated by the dominance of the blue curve over the red curve.

We observed that, for most of the datasets, the aleatoric uncertainties are higher than the epistemic uncertainties, indicating that the primary source of uncertainty in the prediction is related to the inherent random noise in the observations and measurements of the data. While experimental measurements are used in ESOL, FreeSolv, and Lipo datasets, the QM7 dataset rely on density functional theory (DFT), a computational method based on first principles. It is important to note that DFT is a non-deterministic model, with results influenced by multiple factors, such as the choice of exchange-correlation functional, the level of theory employed, the convergence criteria, and numerical approximations [4]. As a result, some degree of uncertainty may be associated with the measurements.

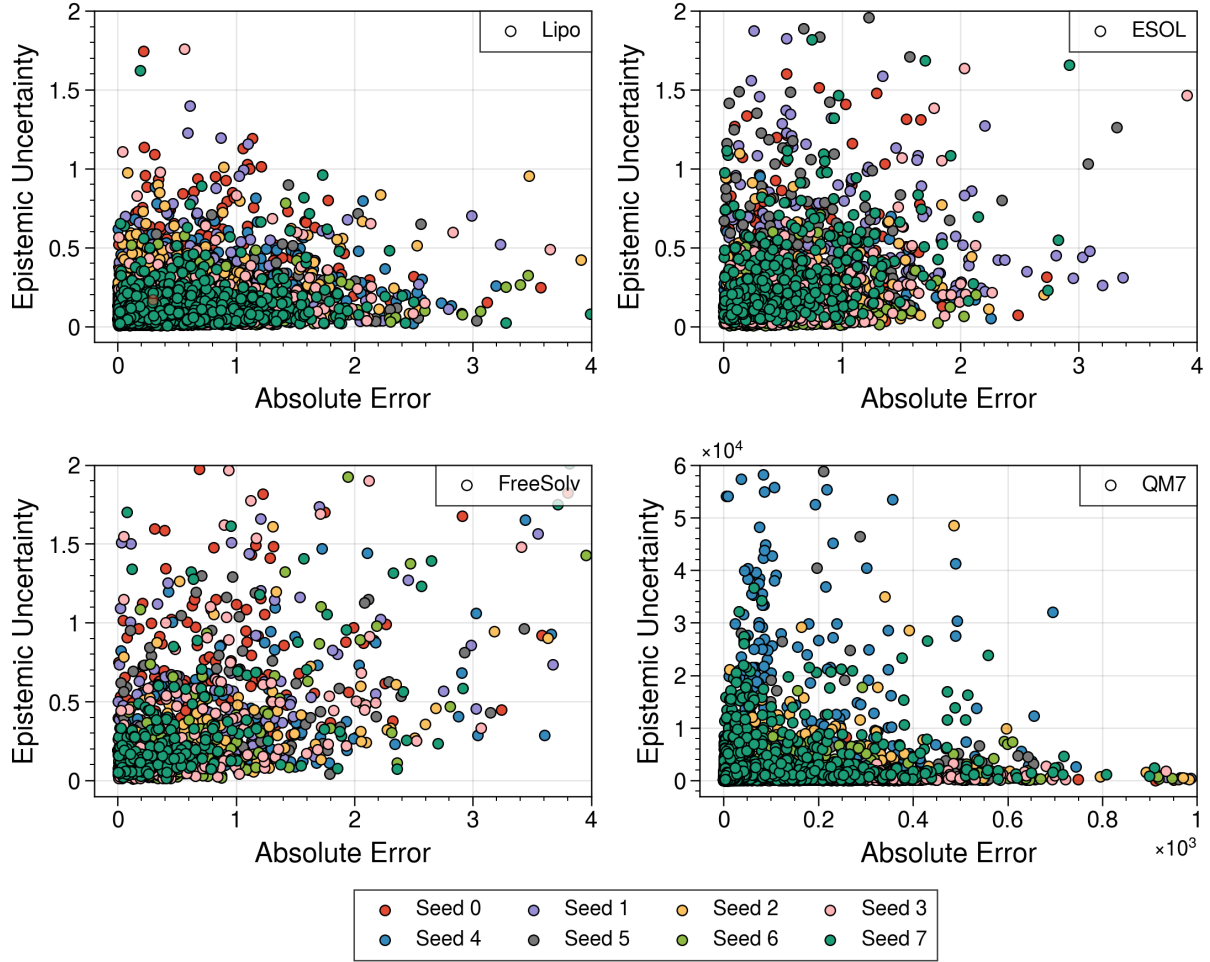


Figure 8: Relationship between epistemic uncertainty and absolute error across eight random seeds. It reveals a trend of increasing uncertainty with higher error. However, there are cases where high error is associated with low uncertainty, or low error with high uncertainty, indicating potential model inadequacy or data limitations.

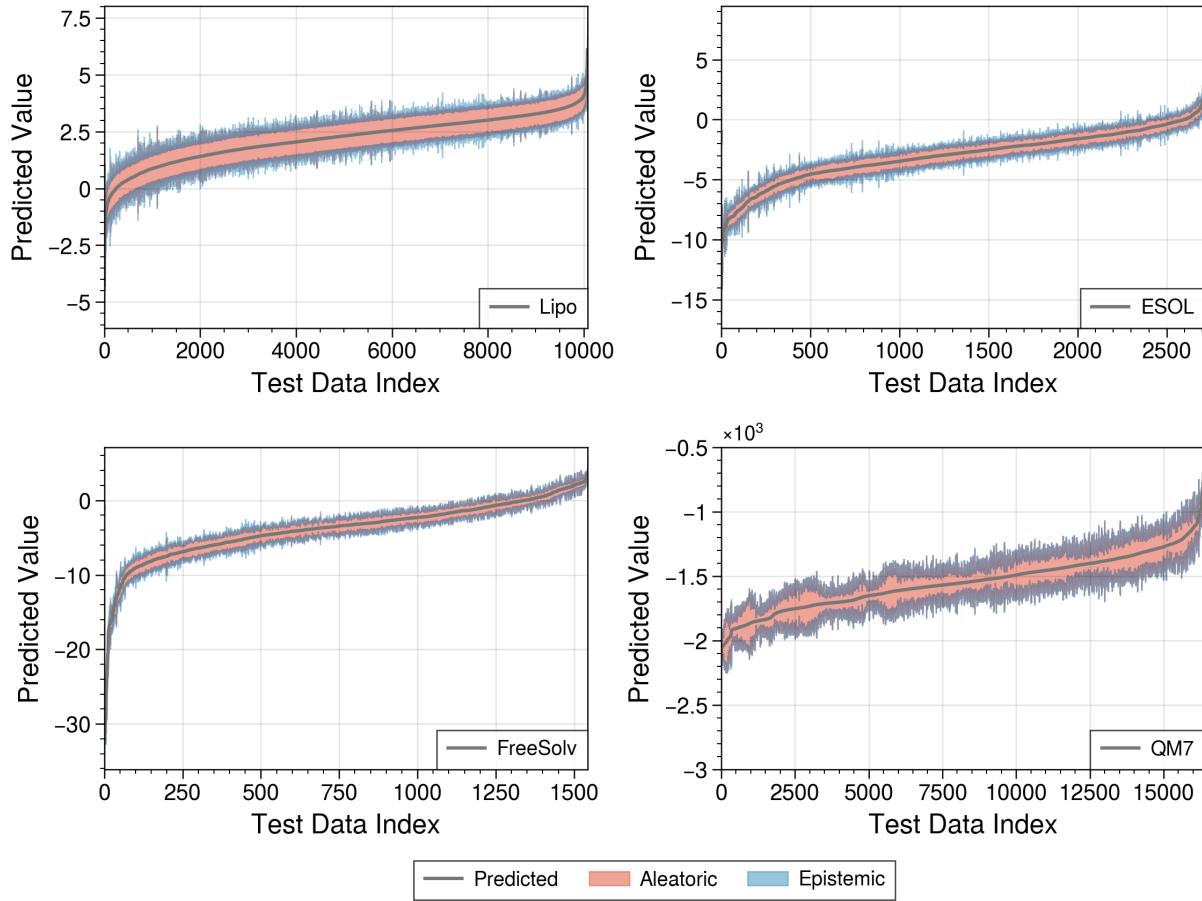


Figure 9: Uncertainty decomposition of all test datasets across eight random seeds. The test data have been ranked by predicted value for visualization purposes. The gray line represents the predicted values, while the red region depicts the aleatoric uncertainty and the blue region shows the epistemic uncertainty.

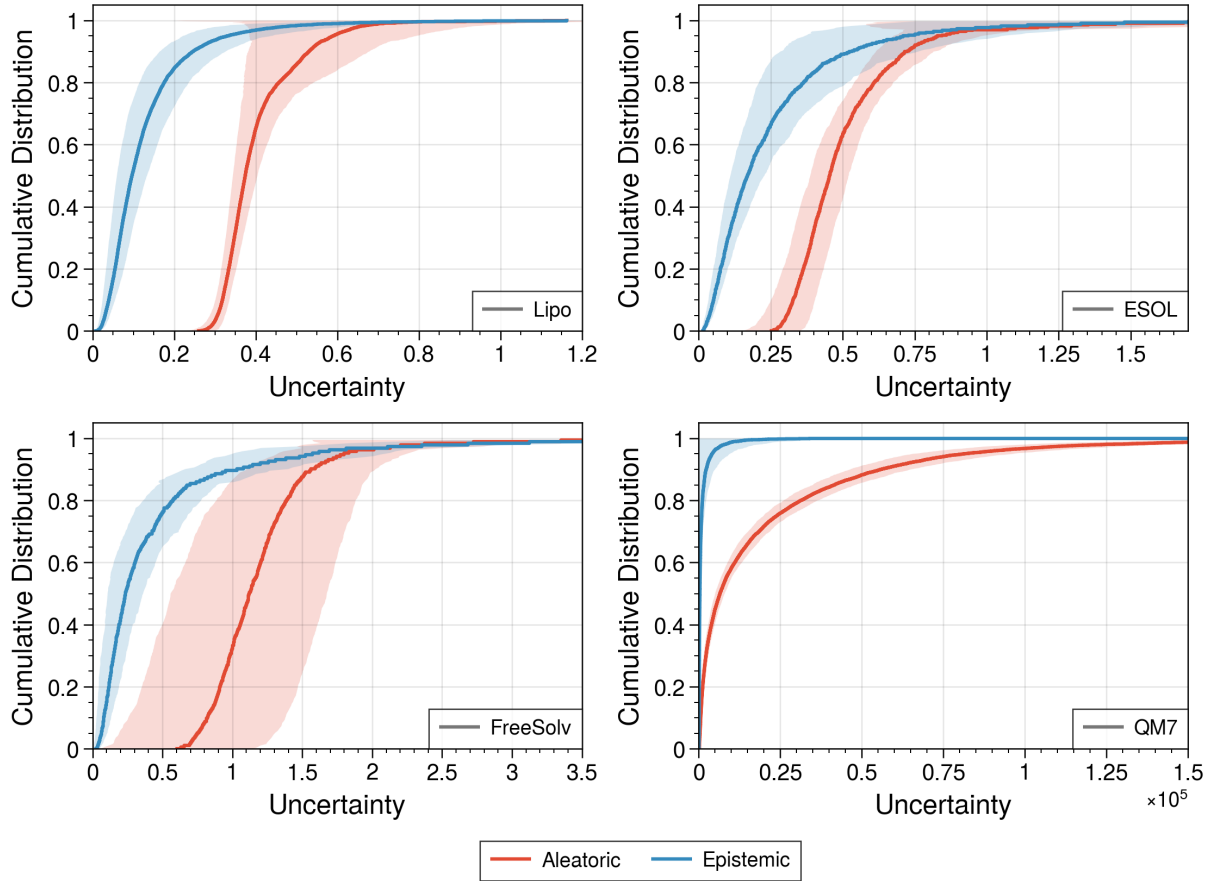


Figure 10: Cumulative density distribution of uncertainty decomposition of all test datasets across eight random seeds. The solid line within the distribution represents the mean, while the shaded area signifies the standard deviation. For all datasets, the curve representing epistemic uncertainty is above the curve of aleatoric uncertainty, indicating that most of the uncertainties in the predictions arise from aleatoric uncertainty.

3.4 Molecular Uncertainties

To address the presence of epistemic uncertainties in `AutoGNNUQ`, we investigated the molecular characteristics and functional groups that contribute to these uncertainties. By analyzing these factors, we have a potential to improve the representation of the molecules and subsequently reduce the uncertainties. To accomplish this, we used MACCS (Molecular ACCESS System) keys [7], which are binary fingerprints that represent each molecule in our dataset by encoding the presence or absence of particular functional groups and substructures. These functional groups include characteristics, such as actinide (index 4), hydroxyl group (index 139), multiple nitrogen atoms (index 142). By analyzing the contribution of each functional group to high epistemic uncertainties, we can gain a better understanding of the impact of individual groups on molecular properties and improve the overall representation of the molecules.

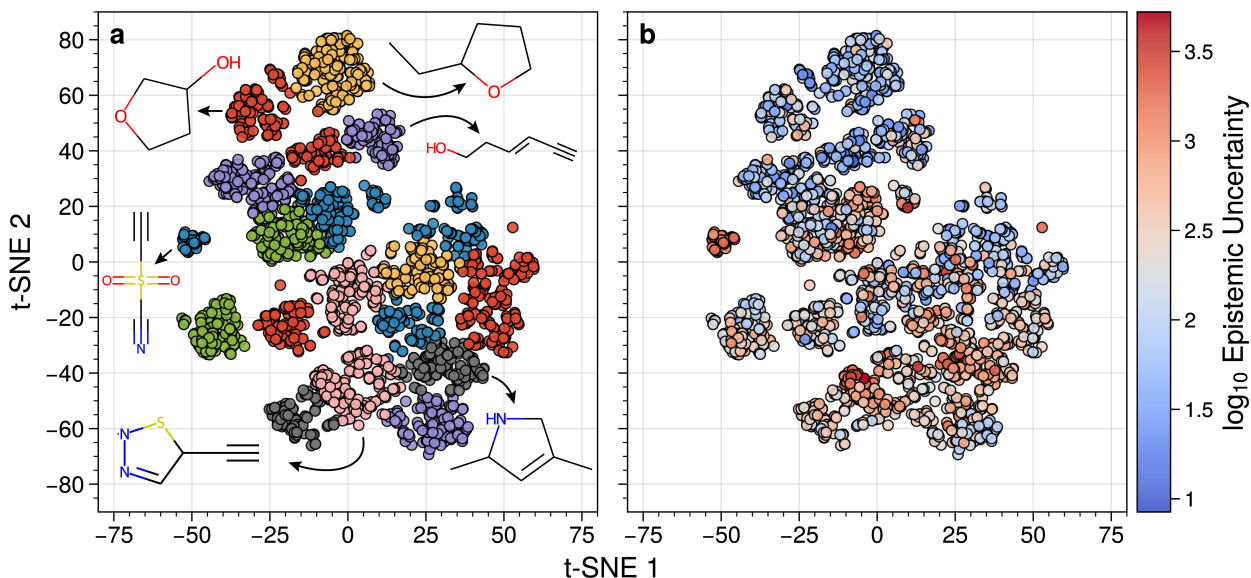


Figure 11: t-SNE plot of the MACCS keys of the test dataset. (a) Clustering by k-means algorithm with $k=20$. (b) Epistemic uncertainties associated with each molecule. Low uncertainties are represented in blue and high uncertainties in red. Some clusters in (a) have low uncertainties (*e.g.*, top clusters), while others have high uncertainties (*e.g.*, bottom clusters).

We utilized t-SNE (t-Distributed Stochastic Neighbor Embedding) [39] to visualize the relationship between the MACCS key vectors and the molecules. The t-SNE algorithm creates probability distributions for the similarities between the high-dimensional data points and the low-dimensional space, optimizing the latter to closely match the former. By mapping the 166-dimensional vectors of all molecules into two dimensions using t-SNE, we can create a plot that can reveal patterns and clusters within complex datasets. This enables us to identify relationships between the molecules and the functional groups that make up their MACCS key vectors. In Figure 11a, we show the t-SNE plot of the QM7 dataset (random seed is 0) and K-means clustering. In Figure 11b, we show the t-SNE plot of the QM7 dataset with associated epistemic uncertainties. We focus on epistemic uncertainties as

they can be reduced by improving data representation and increasing the number of molecules in a specific region of the input space. The results presented in Figure 11 indicate that molecules with low epistemic uncertainties are predominantly comprised of O-heterocycles and hydroxyl groups, while those with high epistemic uncertainties are largely composed of N-heterocycles and sulfonyl groups. This suggests that it is worthwhile to take a closer look at molecules containing N-heterocycles and sulfonyl groups to determine if there are any limitations with the underlying DFT calculation. Additional t-SNE results for various datasets, conducted with differing random seeds, are provided in SI Figures S11 through S18.

4 Conclusions and Future Work

In summary, this paper presents `AutoGNNUQ`, a novel technique for uncertainty quantification in machine learning models used for molecular prediction. `AutoGNNUQ` leverages an aging evolution approach to construct a diverse graph neural network ensemble that models epistemic uncertainty while preserving aleatoric uncertainty quality. Our experiments on several benchmark datasets demonstrate that `AutoGNNUQ` outperforms existing methods in terms of prediction accuracy and uncertainty quantification. By decomposing aleatoric and epistemic uncertainty, we gain valuable insights into areas for reducing uncertainty, and t-SNE visualization enhances our understanding of the correlation between molecular features and uncertainties.

Moving forward, we plan to delve into the specific causes of epistemic uncertainty, including imbalanced data, insufficient representations, and poor models. Additionally, we intend to expand our approach to tackle uncertainty quantification in classification problems and other domains beyond molecular properties. Overall, `AutoGNNUQ` presents a promising direction for improving the accuracy and reliability of machine learning models in various applications. The results of this study highlight the potential of `AutoGNNUQ` to advance the field of uncertainty quantification in machine learning models, particularly in molecular prediction.

Acknowledgments

This material is based on work supported by the U.S. Department of Energy (DOE), Office of Science, Office of Advanced Scientific Computing Research, under Contract DE-AC02-06CH11357. We also acknowledge partial funding from the U.S. National Science Foundation (NSF) under BIGDATA grant IIS-1837812.

Code Availability

The data and code used to generate results are available at <https://github.com/zavalab/ML/tree/master/AUTOGNNUQ>.

References

- [1] Martín Abadi, Paul Barham, Jianmin Chen, Zhifeng Chen, Andy Davis, Jeffrey Dean, Matthieu Devin, Sanjay Ghemawat, Geoffrey Irving, Michael Isard, et al. Tensorflow: a system for large-scale machine learning. In *Osdi*, volume 16, pages 265–283. Savannah, GA, USA, 2016.
- [2] Prasanna Balaprakash, Michael Salim, Thomas D Uram, Venkat Vishwanath, and Stefan M Wild. Deephyper: Asynchronous hyperparameter search for deep neural networks. In *2018 IEEE 25th international conference on high performance computing (HiPC)*, pages 42–51. IEEE, 2018.
- [3] Lorenz C Blum and Jean-Louis Reymond. 970 million druglike small molecules for virtual screening in the chemical universe database gdb-13. *Journal of the American Chemical Society*, 131(25):8732–8733, 2009.
- [4] Kieron Burke. Perspective on density functional theory. *The Journal of chemical physics*, 136(15):150901, 2012.
- [5] Artem Cherkasov, Eugene N Muratov, Denis Fourches, Alexandre Varnek, Igor I Baskin, Mark Cronin, John Dearden, Paola Gramatica, Yvonne C Martin, Roberto Todeschini, et al. Qsar modeling: where have you been? where are you going to? *Journal of medicinal chemistry*, 57(12):4977–5010, 2014.
- [6] John S Delaney. Esol: estimating aqueous solubility directly from molecular structure. *Journal of chemical information and computer sciences*, 44(3):1000–1005, 2004.
- [7] Joseph L Durant, Burton A Leland, Douglas R Henry, and James G Nourse. Reoptimization of mdl keys for use in drug discovery. *Journal of chemical information and computer sciences*, 42(6):1273–1280, 2002.
- [8] Romain Egele, Romit Maulik, Krishnan Raghavan, Prasanna Balaprakash, and Bethany Lusch. Autodeuq: Automated deep ensemble with uncertainty quantification. *arXiv preprint arXiv:2110.13511*, 2021.
- [9] Evan N Feinberg, Debnil Sur, Zhenqin Wu, Brooke E Husic, Huanghao Mai, Yang Li, Saisai Sun, Jianyi Yang, Bharath Ramsundar, and Vijay S Pande. Potentialnet for molecular property prediction. *ACS central science*, 4(11):1520–1530, 2018.
- [10] Yarin Gal and Zoubin Ghahramani. Bayesian convolutional neural networks with bernoulli approximate variational inference. *arXiv preprint arXiv:1506.02158*, 2015.
- [11] Yarin Gal and Zoubin Ghahramani. Dropout as a bayesian approximation: Representing model uncertainty in deep learning. In *international conference on machine learning*, pages 1050–1059. PMLR, 2016.
- [12] Yarin Gal, Jiri Hron, and Alex Kendall. Concrete dropout. *Advances in neural information processing systems*, 30, 2017.

- [13] Jakob Gawlikowski, Cedrique Rovile Njietcheu Tassi, Mohsin Ali, Jongseok Lee, Matthias Humt, Jianxiang Feng, Anna Kruspe, Rudolph Triebel, Peter Jung, Ribana Roscher, et al. A survey of uncertainty in deep neural networks. *arXiv preprint arXiv:2107.03342*, 2021.
- [14] Justin Gilmer, Samuel S Schoenholz, Patrick F Riley, Oriol Vinyals, and George E Dahl. Neural message passing for quantum chemistry. In *International conference on machine learning*, pages 1263–1272. PMLR, 2017.
- [15] Daniele Grattarola and Cesare Alippi. Graph neural networks in tensorflow and keras with spektral [application notes]. *IEEE Computational Intelligence Magazine*, 16(1):99–106, 2021.
- [16] Roger Grosse and James Martens. A kronecker-factored approximate fisher matrix for convolution layers. In *International Conference on Machine Learning*, pages 573–582. PMLR, 2016.
- [17] Lars Kai Hansen and Peter Salamon. Neural network ensembles. *IEEE transactions on pattern analysis and machine intelligence*, 12(10):993–1001, 1990.
- [18] Zhongkai Hao, Chengqiang Lu, Zhenya Huang, Hao Wang, Zheyuan Hu, Qi Liu, Enhong Chen, and Cheekong Lee. Asgn: An active semi-supervised graph neural network for molecular property prediction. In *Proceedings of the 26th ACM SIGKDD International Conference on Knowledge Discovery & Data Mining*, pages 731–752, 2020.
- [19] Emily J Herron, Steven R Young, and Thomas E Potok. Ensembles of networks produced from neural architecture search. In *High Performance Computing: ISC High Performance 2020 International Workshops, Frankfurt, Germany, June 21–25, 2020, Revised Selected Papers 35*, pages 223–234. Springer, 2020.
- [20] Lior Hirschfeld, Kyle Swanson, Kevin Yang, Regina Barzilay, and Connor W Coley. Uncertainty quantification using neural networks for molecular property prediction. *Journal of Chemical Information and Modeling*, 60(8):3770–3780, 2020.
- [21] Shubham Jain and Sriji PK. Monte carlo dropout based batchensemble for improving uncertainty estimation. In *Proceedings of the 6th Joint International Conference on Data Science & Management of Data (10th ACM IKDD CODS and 28th COMAD)*, pages 138–138, 2023.
- [22] Jon Paul Janet, Chenru Duan, Tzuhsiung Yang, Aditya Nandy, and Heather J Kulik. A quantitative uncertainty metric controls error in neural network-driven chemical discovery. *Chemical science*, 10(34):7913–7922, 2019.
- [23] Shengli Jiang and Prasanna Balaprakash. Graph neural network architecture search for molecular property prediction. In *2020 IEEE International conference on big data (big data)*, pages 1346–1353. IEEE, 2020.
- [24] Diederik P Kingma and Jimmy Ba. Adam: A method for stochastic optimization. *arXiv preprint arXiv:1412.6980*, 2014.

- [25] Balaji Lakshminarayanan, Alexander Pritzel, and Charles Blundell. Simple and scalable predictive uncertainty estimation using deep ensembles. *Advances in neural information processing systems*, 30, 2017.
- [26] Jongseok Lee, Matthias Humt, Jianxiang Feng, and Rudolph Triebel. Estimating model uncertainty of neural networks in sparse information form. In *International Conference on Machine Learning*, pages 5702–5713. PMLR, 2020.
- [27] Ioannis E Livieris, Lazaros Iliadis, and Panagiotis Pintelas. On ensemble techniques of weight-constrained neural networks. *Evolving Systems*, 12:155–167, 2021.
- [28] Artem Lysenko, Alok Sharma, Keith A Boroevich, and Tatsuhiko Tsunoda. An integrative machine learning approach for prediction of toxicity-related drug safety. *Life science alliance*, 1(6), 2018.
- [29] Romit Maulik, Romain Egele, Bethany Lusch, and Prasanna Balaprakash. Recurrent neural network architecture search for geophysical emulation. In *SC20: International Conference for High Performance Computing, Networking, Storage and Analysis*, pages 1–14. IEEE, 2020.
- [30] David Mendez, Anna Gaulton, A Patrícia Bento, Jon Chambers, Marleen De Veij, Eloy Félix, María Paula Magariños, Juan F Mosquera, Prudence Mutowo, Michał Nowotka, et al. ChEMBL: towards direct deposition of bioassay data. *Nucleic acids research*, 47(D1):D930–D940, 2019.
- [31] David L Mobley and J Peter Guthrie. Freesolv: a database of experimental and calculated hydration free energies, with input files. *Journal of computer-aided molecular design*, 28:711–720, 2014.
- [32] Grégoire Montavon, Matthias Rupp, Vivekanand Gobre, Alvaro Vazquez-Mayagoitia, Katja Hansen, Alexandre Tkatchenko, Klaus-Robert Müller, and O Anatole Von Lilienfeld. Machine learning of molecular electronic properties in chemical compound space. *New Journal of Physics*, 15(9):095003, 2013.
- [33] David A Nix and Andreas S Weigend. Estimating the mean and variance of the target probability distribution. In *Proceedings of 1994 IEEE international conference on neural networks (ICNN'94)*, volume 1, pages 55–60. IEEE, 1994.
- [34] Fabian Pedregosa, Gaël Varoquaux, Alexandre Gramfort, Vincent Michel, Bertrand Thirion, Olivier Grisel, Mathieu Blondel, Peter Prettenhofer, Ron Weiss, Vincent Dubourg, et al. Scikit-learn: Machine learning in python. *the Journal of machine Learning research*, 12:2825–2830, 2011.
- [35] Apostolos F Psaros, Xuhui Meng, Zongren Zou, Ling Guo, and George Em Karniadakis. Uncertainty quantification in scientific machine learning: Methods, metrics, and comparisons. *Journal of Computational Physics*, page 111902, 2023.
- [36] Esteban Real, Alok Aggarwal, Yanping Huang, and Quoc V Le. Regularized evolution for image classifier architecture search. In *Proceedings of the AAAI conference on artificial intelligence*, volume 33, pages 4780–4789, 2019.

- [37] Hippolyt Ritter, Aleksandar Botev, and David Barber. A scalable laplace approximation for neural networks. In *6th International Conference on Learning Representations, ICLR 2018-Conference Track Proceedings*, volume 6. International Conference on Representation Learning, 2018.
- [38] Kevin Tran, Willie Neiswanger, Junwoong Yoon, Qingyang Zhang, Eric Xing, and Zachary W Ulissi. Methods for comparing uncertainty quantifications for material property predictions. *Machine Learning: Science and Technology*, 1(2):025006, 2020.
- [39] Laurens Van der Maaten and Geoffrey Hinton. Visualizing data using t-sne. *Journal of machine learning research*, 9(11), 2008.
- [40] Petar Veličković, Guillem Cucurull, Arantxa Casanova, Adriana Romero, Pietro Lio, and Yoshua Bengio. Graph attention networks. *arXiv preprint arXiv:1710.10903*, 2017.
- [41] W Patrick Walters and Regina Barzilay. Applications of deep learning in molecule generation and molecular property prediction. *Accounts of chemical research*, 54(2):263–270, 2020.
- [42] Zhenqin Wu, Bharath Ramsundar, Evan N Feinberg, Joseph Gomes, Caleb Geniesse, Aneesh S Pappu, Karl Leswing, and Vijay Pande. Moleculenet: a benchmark for molecular machine learning. *Chemical science*, 9(2):513–530, 2018.
- [43] Keyulu Xu, Weihua Hu, Jure Leskovec, and Stefanie Jegelka. How powerful are graph neural networks? *arXiv preprint arXiv:1810.00826*, 2018.

Uncertainty Quantification for Molecular Property Predictions with Graph Neural Architecture Search

Shengli Jiang^{1*}, Shiyi Qin¹, Reid C. Van Lehn¹, Prasanna Balaprakash² and Victor M. Zavala^{1,3}

¹Department of Chemical and Biological Engineering

University of Wisconsin-Madison, 1415 Engineering Dr, Madison, WI 53706

²Computing and Computational Sciences Directorate

Oak Ridge National Laboratory, P.O. Box 2008, Oak Ridge, TN 37831

³Mathematics and Computer Science Division

Argonne National Laboratory, Lemont, IL 60439

S1 AutoGNNUQ

S1.1 Attention Functions

The attention functions used to calculate α_{vw} are shown in Table S1. For constant attention, α_{vw} is always 1. For GAT, α_{vw} is $\text{LeakyReLU}(\mathbf{a}(\mathbf{W}\mathbf{h}_v || \mathbf{W}\mathbf{h}_w))$, where \mathbf{a} is a trainable vector, \mathbf{W} is a trainable weight matrix, $||$ denotes concatenation, and \mathbf{h}_v and \mathbf{h}_w are the node hidden feature vectors for nodes v and w , respectively. The SYM-GAT attention coefficient is procured by the summation of α_{vw} and α_{wv} from GAT. The COS attention type computes α_{vw} as $\mathbf{a}(\mathbf{W}\mathbf{h}_v || \mathbf{W}\mathbf{h}_w)$. In linear attention, α_{vw} is $\tanh(\mathbf{a}_l \mathbf{W}\mathbf{h}_v + \mathbf{W}\mathbf{h}_w)$, with \mathbf{a}_l being a learnable vector. Generalized linear attention, or gen-linear attention, determines α_{vw} as $\mathbf{W}_G \tanh(\mathbf{W}\mathbf{h}_v + \mathbf{W}\mathbf{h}_w)$, where \mathbf{W}_G is a trainable matrix.

S1.2 Architectures Discovered

Figure S1 presents the optimal model architectures identified for the Lipo dataset using a random seed of 0, while Figure S2 depicts the least effective models. In this context, input 0 corresponds to node features, input 1 to edge features, input 2 to edge pairs, and input 3 to node masks. A clear observation is that superior models generally incorporate more skip-connections and predominantly use the global attention pooling function. Conversely, the less effective models exhibit simpler architectures with rudimentary readout functions such as global sum pooling and global max pooling.

*Corresponding Author: sjiang87@wisc.edu

Table S1: Set of attention functions, where \parallel denotes the concatenation; \mathbf{a} , \mathbf{a}_l , and \mathbf{a}_r ; and \mathbf{W}_G is a trainable matrix.

Attention Mechanism	Equations
Constant	1
GAT	$\text{LeakyReLU}(\mathbf{a}(\mathbf{W}\mathbf{h}_v \parallel \mathbf{W}\mathbf{h}_w))$
SYM-GAT	$\alpha_{vw} + \alpha_{wv}$ based on GAT
COS	$\mathbf{a}(\mathbf{W}\mathbf{h}_v \parallel \mathbf{W}\mathbf{h}_w)$
Linear	$\tanh(\mathbf{a}_l \mathbf{W}\mathbf{h}_v + \mathbf{W}\mathbf{h}_w)$
Gen-Linear	$\mathbf{W}_G \tanh(\mathbf{W}\mathbf{h}_v + \mathbf{W}\mathbf{h}_w)$

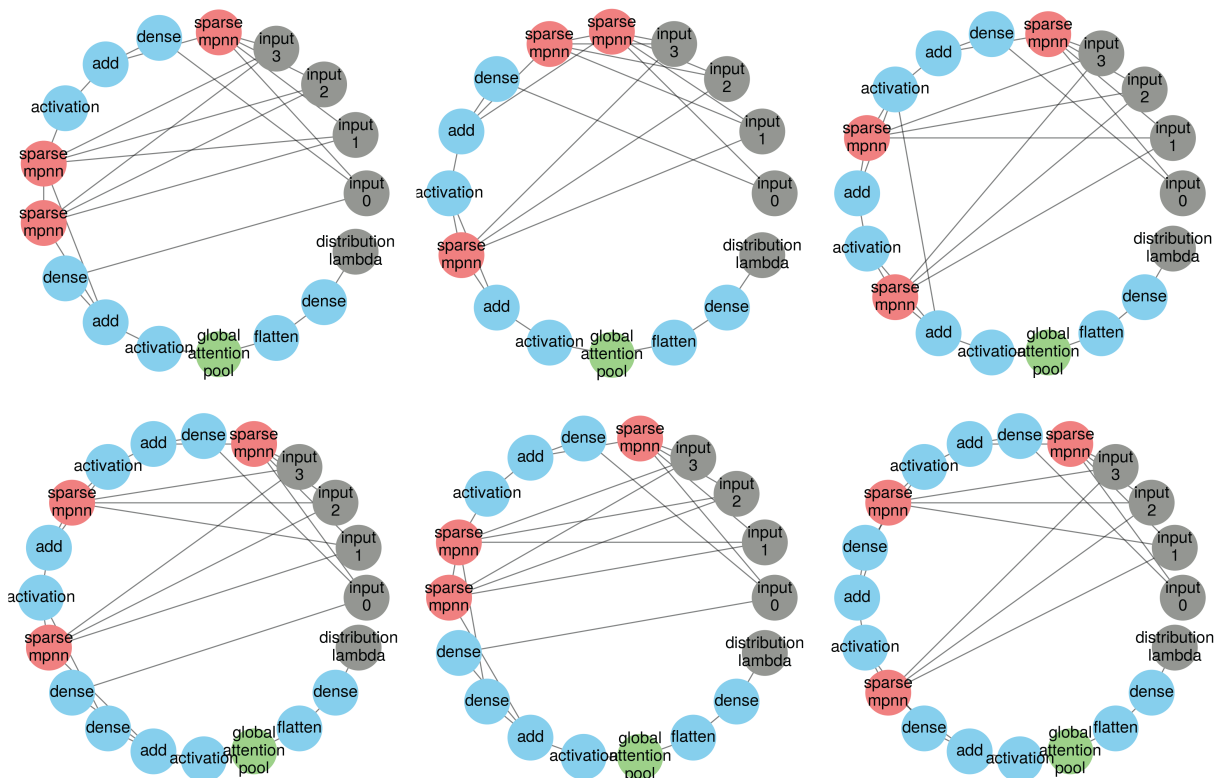


Figure S1: Six model architectures demonstrating the highest search rewards (log-likelihood) for the Lipo dataset, using a random seed of 0.

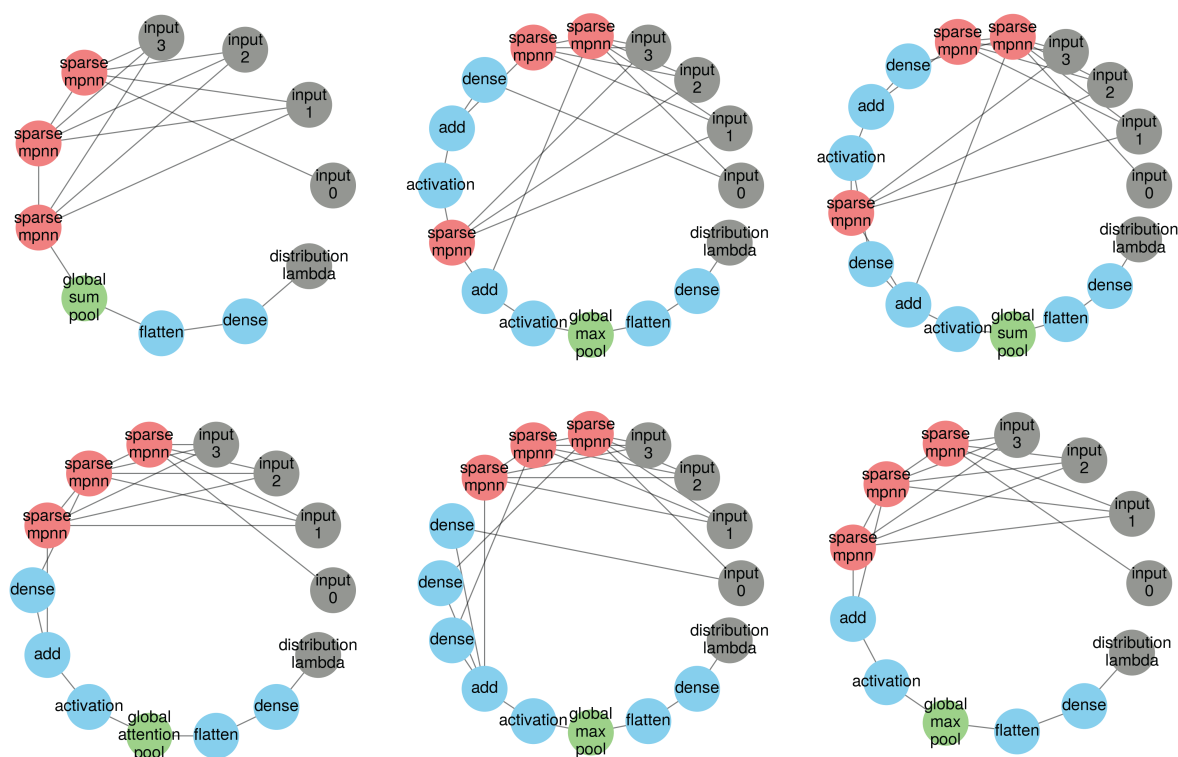


Figure S2: Six model architectures demonstrating the lowest search rewards (log-likelihood) for the Lipo dataset, using a random seed of 0.

S2 Results

S2.1 Searching Reward

Figures S3-S10 present the search rewards corresponding to each random seed employed in the data splitting process across the four datasets. Notwithstanding the inherent stochasticity introduced by the random seeds and searching algorithm, the search across all datasets converges after 300 evaluations.

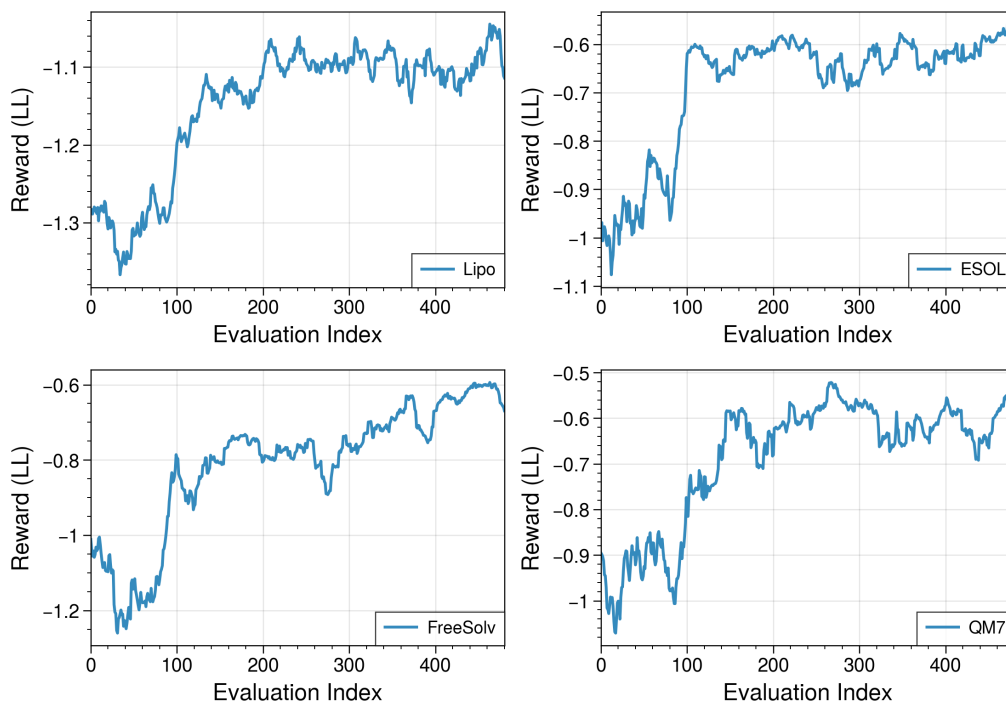


Figure S3: Search trajectories represented for all datasets for random seed 0.

S2.2 TSNE

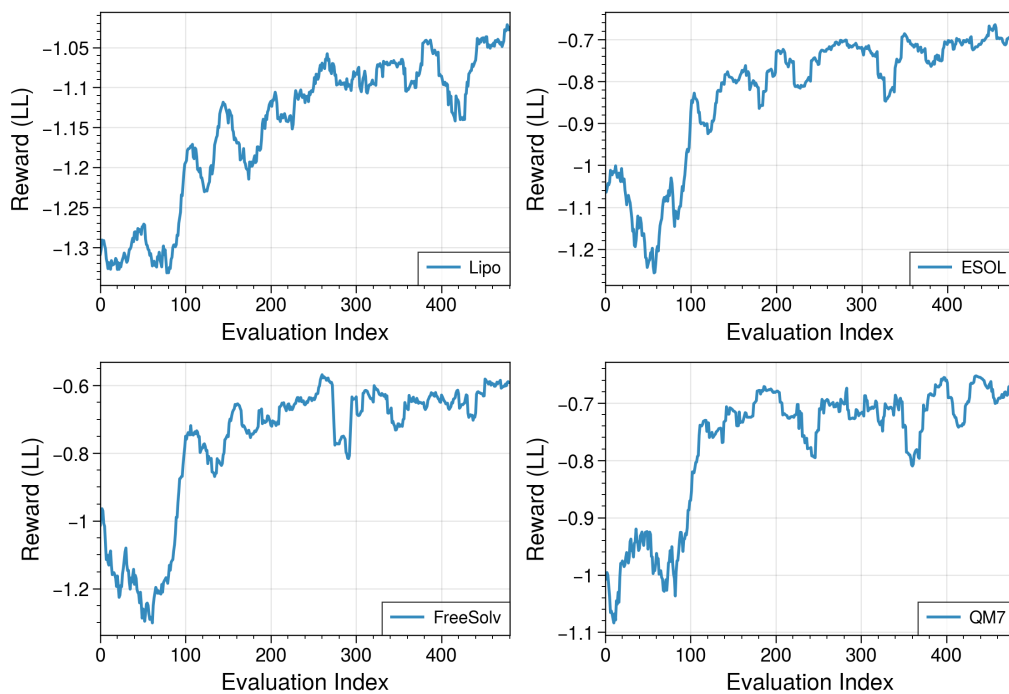


Figure S4: Search trajectories represented for all datasets for random seed 1.

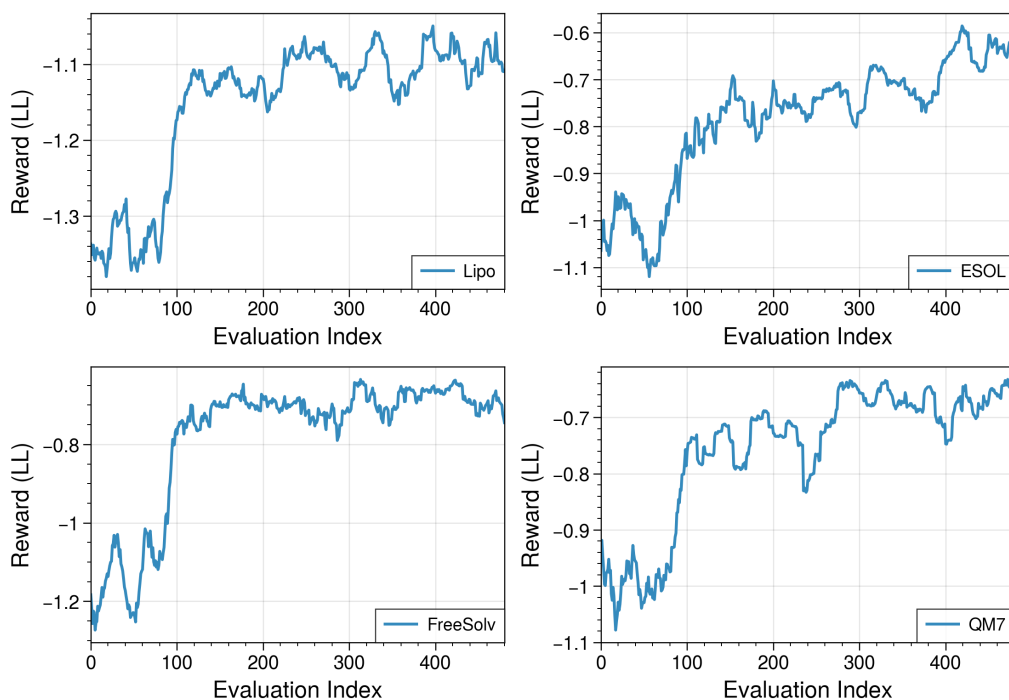


Figure S5: Search trajectories represented for all datasets for random seed 2.

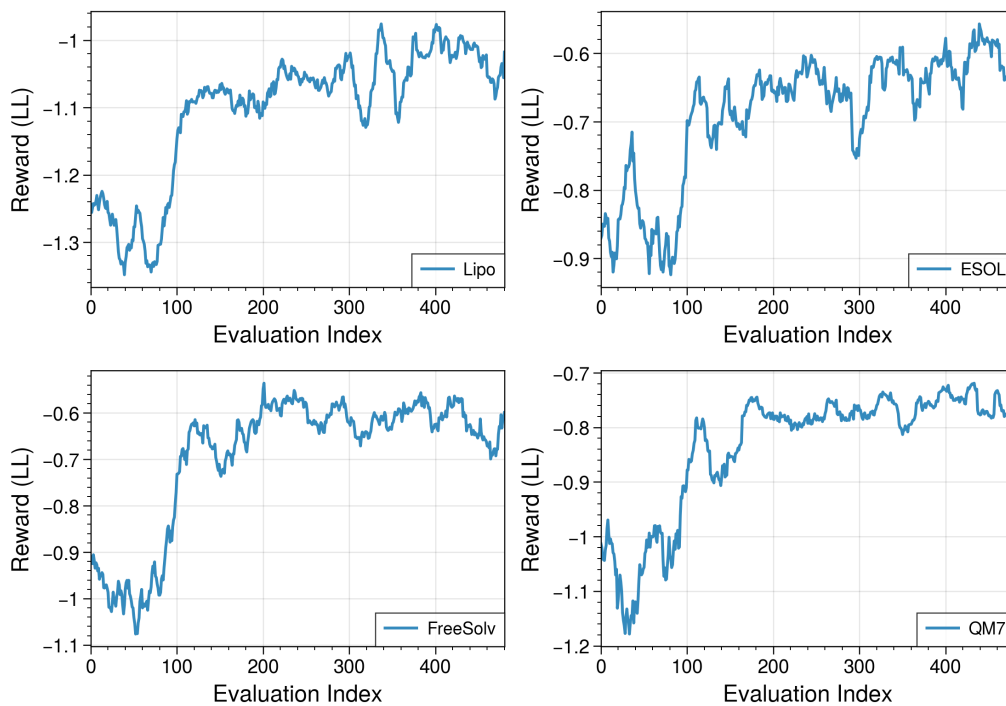


Figure S6: Search trajectories represented for all datasets for random seed 3.

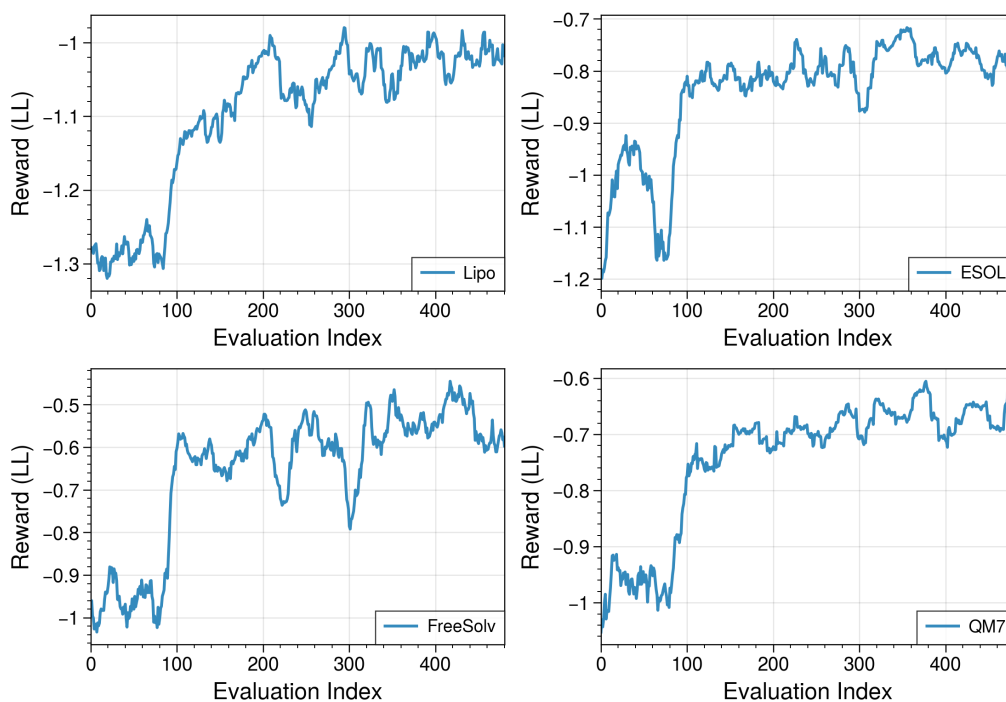


Figure S7: Search trajectories represented for all datasets for random seed 4.

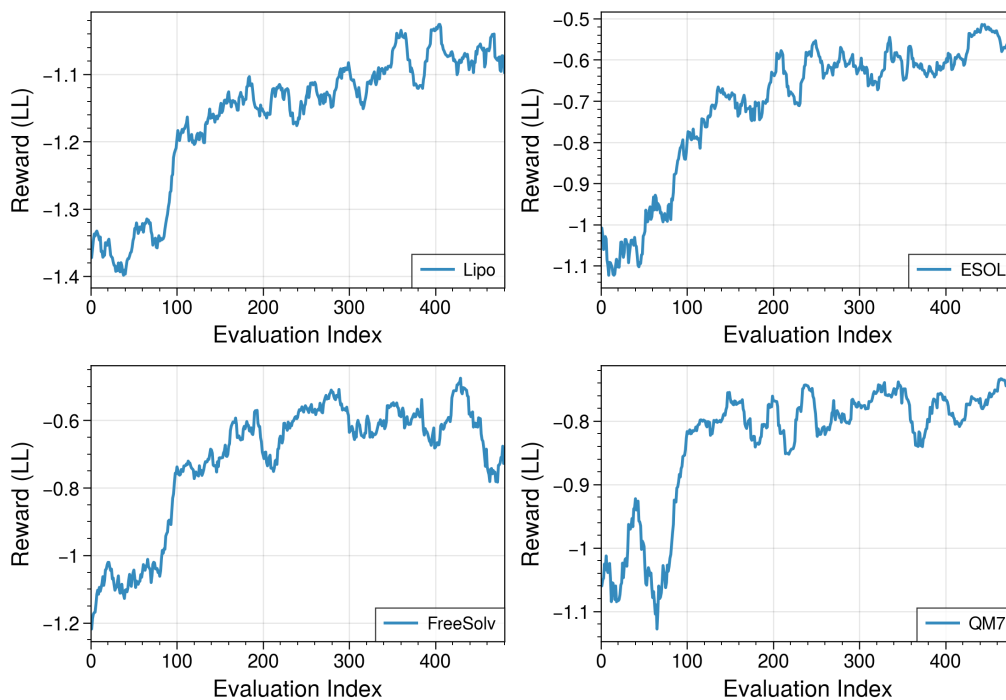


Figure S8: Search trajectories represented for all datasets for random seed 5.

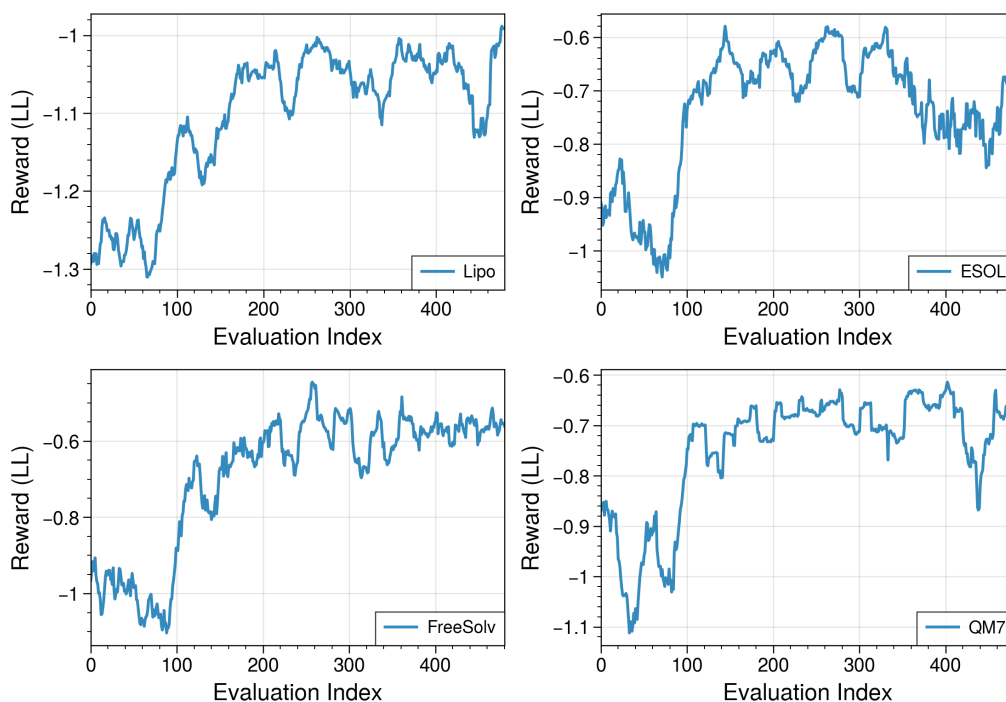


Figure S9: Search trajectories represented for all datasets for random seed 6.

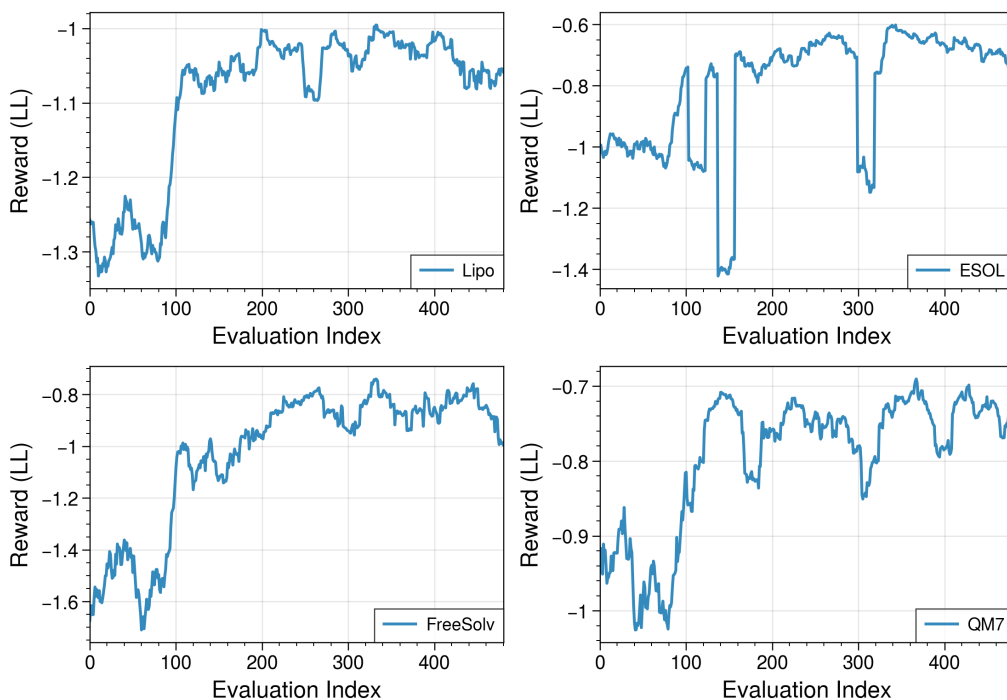


Figure S10: Search trajectories represented for all datasets for random seed 7.

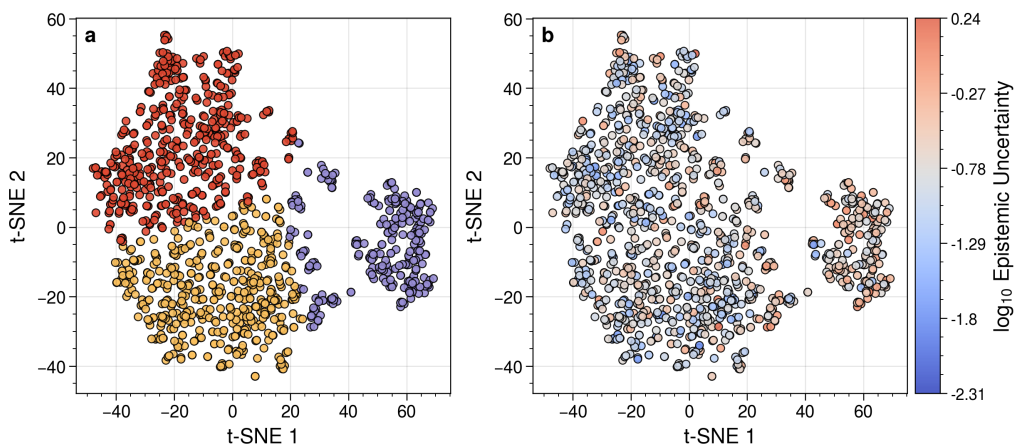


Figure S11: t-SNE plot of Lipo MACCS keys for random seed 0. (a) Clustering by k-means algorithm. (b) Epistemic uncertainties associated with each molecule. Low uncertainties are represented in blue and high uncertainties in red.

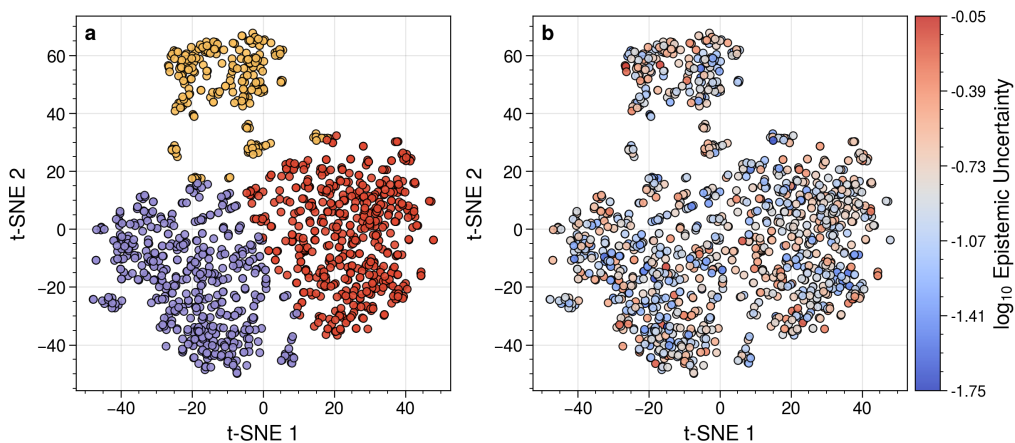


Figure S12: t-SNE plot of Lipo MACCS keys for random seed 1. (a) Clustering by k-means algorithm. (b) Epistemic uncertainties associated with each molecule. Low uncertainties are represented in blue and high uncertainties in red.

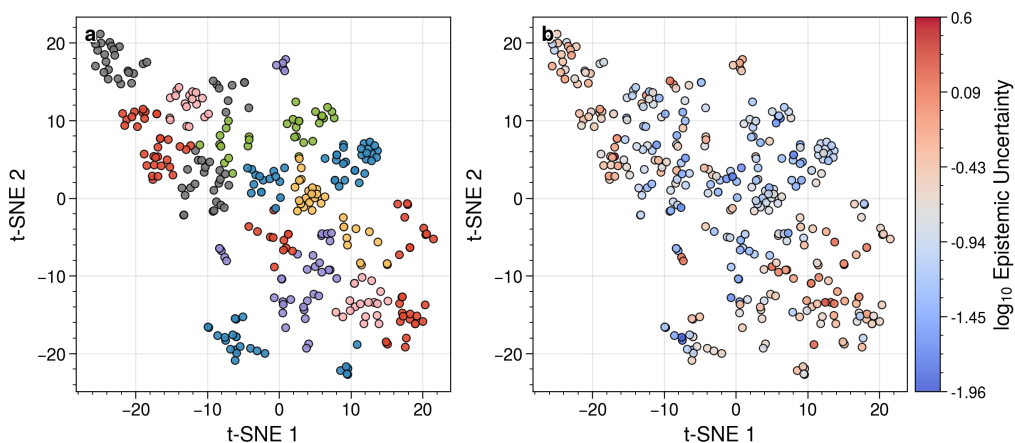


Figure S13: t-SNE plot of ESOL MACCS keys for random seed 0. (a) Clustering by k-means algorithm. (b) Epistemic uncertainties associated with each molecule. Low uncertainties are represented in blue and high uncertainties in red.

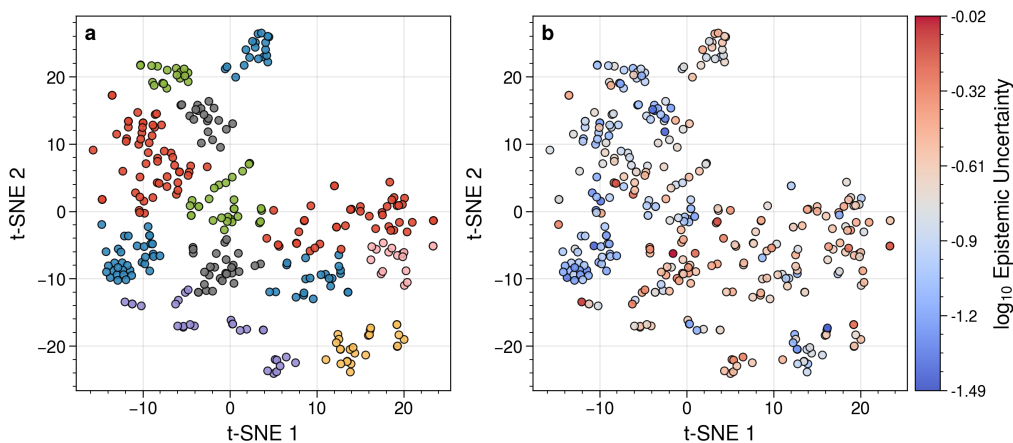


Figure S14: t-SNE plot of ESOL MACCS keys for random seed 1. (a) Clustering by k-means algorithm. (b) Epistemic uncertainties associated with each molecule. Low uncertainties are represented in blue and high uncertainties in red.

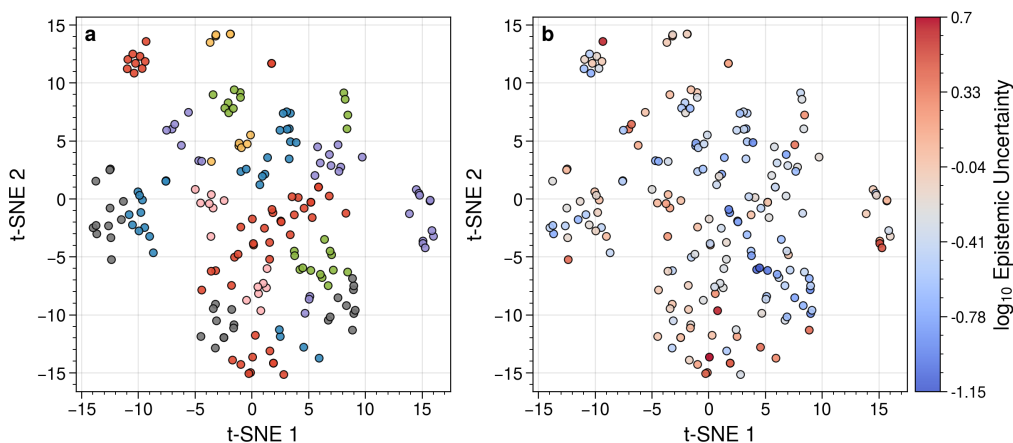


Figure S15: t-SNE plot of FreeSolv MACCS keys for random seed 0. (a) Clustering by k-means algorithm. (b) Epistemic uncertainties associated with each molecule. Low uncertainties are represented in blue and high uncertainties in red.

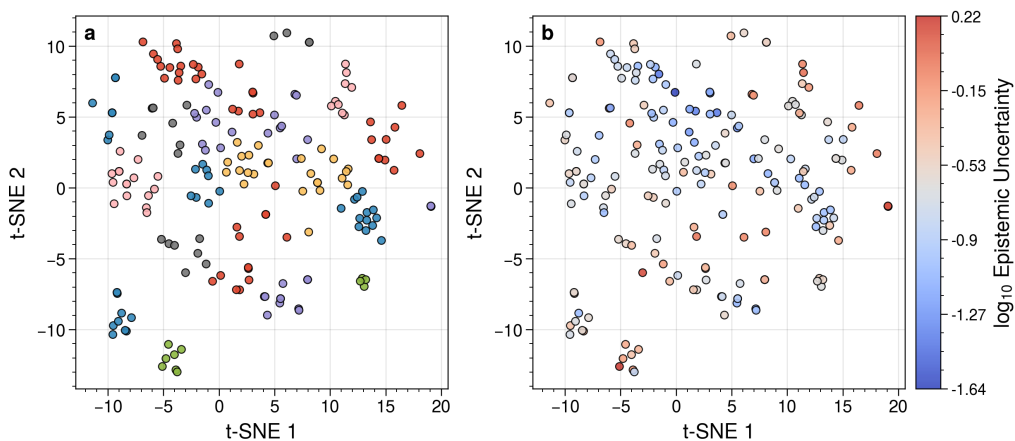


Figure S16: t-SNE plot of FreeSolv MACCS keys for random seed 1. (a) Clustering by k-means algorithm. (b) Epistemic uncertainties associated with each molecule. Low uncertainties are represented in blue and high uncertainties in red.

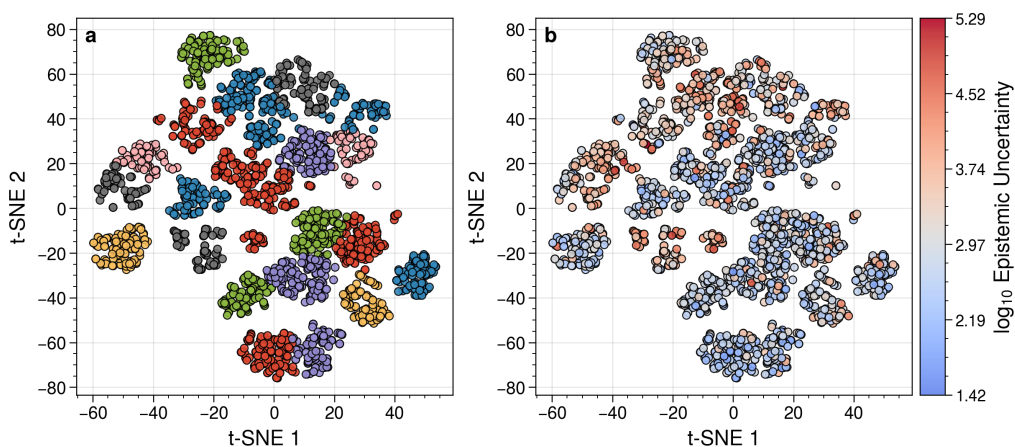


Figure S17: t-SNE plot of QM7 MACCS keys for random seed 1. (a) Clustering by k-means algorithm. (b) Epistemic uncertainties associated with each molecule. Low uncertainties are represented in blue and high uncertainties in red.

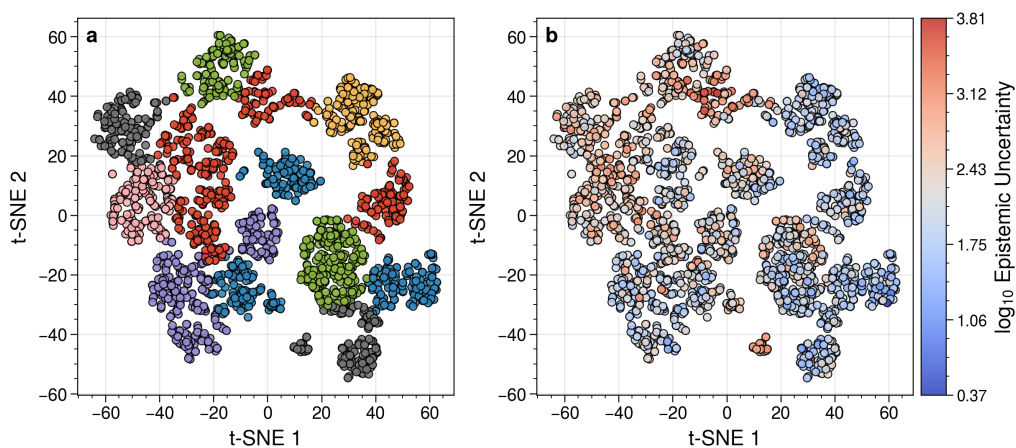


Figure S18: t-SNE plot of QM7 MACCS keys for random seed 2. (a) Clustering by k-means algorithm. (b) Epistemic uncertainties associated with each molecule. Low uncertainties are represented in blue and high uncertainties in red.